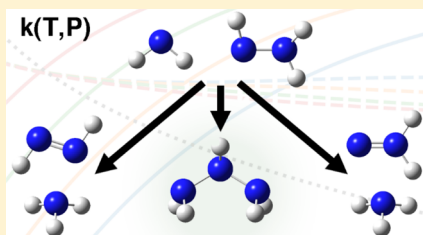


# Large Intermediates in Hydrazine Decomposition: A Theoretical Study of the $N_3H_5$ and $N_4H_6$ Potential Energy Surfaces

Alon Grinberg Dana,<sup>†</sup> Kevin B. Moore, III,<sup>‡</sup> Ahren W. Jasper,<sup>‡</sup> and William H. Green<sup>\*,†</sup><sup>†</sup>Department of Chemical Engineering, Massachusetts Institute of Technology, Cambridge, Massachusetts 02139, United States<sup>‡</sup>Chemical Sciences and Engineering Division, Argonne National Laboratory, Argonne, Illinois 60439, United States

## Supporting Information

**ABSTRACT:** Large complex formation involved in the thermal decomposition of hydrazine ( $N_2H_4$ ) is studied using transition state theory-based theoretical kinetics. A comprehensive analysis of the  $N_3H_5$  and  $N_4H_6$  potential energy surfaces was performed at the CCSD(T)-F12a/aug-cc-pVTZ// $\omega$ B97x-D3/6-311++G(3df,3pd) level of theory, and pressure-dependent rate coefficients were determined. There are no low-barrier unimolecular decomposition pathways for triazane ( $n$ - $N_3H_5$ ), and its formation becomes more significant as the pressure increases; it is the primary product of  $N_2H_3 + NH_2$  below 550, 800, 1150, and 1600 K at 0.1, 1, 10, and 100 bar, respectively. The  $N_4H_6$  surface has two important entry channels,  $N_2H_4 + H_2NN$  and  $N_2H_3 + N_2H_3$ , each with different primary products. Interestingly,  $N_2H_4 + H_2NN$  primarily forms  $N_2H_3 + N_2H_3$ , while disproportionation of  $N_2H_3 + N_2H_3$  predominantly leads to the other  $N_2H_2$  isomer, HNNH. Stabilized tetrazane ( $n$ - $N_4H_6$ ) formation from  $N_2H_3 + N_2H_3$  becomes significant only at relatively high pressures and low temperatures because of fall-off back into  $N_2H_3 + N_2H_3$ . Pressure-dependent rate coefficients for all considered reactions as well as thermodynamic properties of triazane and tetrazane, which should be considered for kinetic modeling of chemical processes involving nitrogen- and hydrogen-containing species, are reported.



## 1. INTRODUCTION

Hydrazine ( $N_2H_4$ ), the main component of diamine-based rocket fuels, is an excellent propellant: using oxygen as the oxidizer, it is only second to hydrogen in terms of the specific impulse (thrust developed per fuel mass per unit time) it generates.<sup>1</sup> Its decomposition could lead to autoignition and detonation,<sup>2–4</sup> and it is sometimes used as a monopropellant, usually by decomposing over a catalyst.<sup>1</sup> Hydrazine and hydrazine-based fuels such as monomethyl hydrazine are more commonly used as bipropellants with  $N_2O_5$  as the oxidizer. Hydrazine is used in thruster engines for attitude and in-orbit control of satellites and spacecraft,<sup>1</sup> where it is being stored and utilized at a maximal pressure of about 25 bar.<sup>5–7</sup>

No detailed kinetic models for hydrazine-based fuel combustion in  $N_2O_5$  exist in the current literature; a step toward this goal is understanding hydrazine decomposition better. Detailed kinetic models for hydrazine decomposition were previously suggested by Halat-Augier et al.<sup>8</sup> as well as by Konnov and De Ruyck.<sup>9</sup> More recently, however, computations of the  $N_2H_2$ ,<sup>10,11</sup>  $N_2H_3$ ,<sup>11</sup> and  $N_2H_4$ <sup>10–12</sup> potential energy surfaces (PESs) determined updated kinetics. Interestingly, none of the previous works on hydrazine decomposition has considered species containing more than two nitrogen atoms. In the absence of an oxidizer, a monopropellant's decomposition could be thought of as an extreme case of fuel-rich combustion, a chemistry region in which fuel-radical recombination reactions often play a significant role. At low pressures, chemically activated isomerization and decompositions are often important. As the working pressure increases,

radical recombination reactions, leading to the formation of relatively large complexes, become more significant because of collisional stabilization.

Unlike carbon, nitrogen does not normally form the major elemental backbone of large molecules. For example, an experimental study of tetrazene (linear unsaturated  $N_4H_4$ ) determined that its thermolysis in the solid phase begins at room temperature, whereas in the gas phase it is metastable.<sup>13</sup> Moreover, cyclic nitrogenous rings, and specifically tetrazetidine (cyclic  $N_4H_4$ ), were determined to have relatively high ring strain energies.<sup>14–16</sup> However, a theoretical study of triazane ( $N_3H_5$ ) concluded that it is kinetically stable.<sup>17</sup> Tetrazane (saturated  $N_4H_6$ ) was also studied theoretically, and its most stable stereoisomer was determined,<sup>18</sup> yet its overall kinetic stability was not assessed. A subatmospheric room-temperature experimental observation of  $N_2H_3$  self-reaction concluded that the disproportionation reaction yielding  $N_2H_4 + N_2H_2$  is approximately four times faster than a recombination reaction yielding tetrazane, unlike the tendency of the analogous hydrocarbon radical,  $C_2H_5$ .<sup>19</sup> Yet, the behavior of the  $N_2H_3 + N_2H_3$  system at high temperatures and different pressures, and specifically the importance of well-skipping chemically activated reactions, has not been reported in the literature.

Received: March 8, 2019

Revised: April 30, 2019

Published: May 2, 2019



In the present contribution, we examine the hypothesis that abundant radicals in decomposing hydrazine might form relatively large complexes such as triazane and tetrazane, becoming more significant as the pressure increases. We therefore explore the  $\text{NH}_2 + \text{N}_2\text{H}_3$  and  $\text{N}_2\text{H}_3 + \text{N}_2\text{H}_3$  reactions which lead to pressure-dependent kinetic networks on the  $\text{N}_3\text{H}_5$  and  $\text{N}_4\text{H}_6$  PESs, respectively. Specifically, collisional-stabilized formation of the complexes along with well-skipping reactions is considered, and pressure-dependent rate coefficients are determined.

## 2. THEORETICAL METHODS

**2.1. Characterization of the PES.** Geometric structures and vibrational frequencies for all wells and saddle points considered here were obtained using density functional theory employing the  $\omega\text{B97x-D3}$  functional<sup>20</sup> and the 6-311++G-(3df,3pd) basis set.<sup>21</sup> Frequencies were scaled by a recommended factor of 0.97027<sup>27</sup> to account for their average overestimation, due in part to anharmonicity. The growing string method (GSM)<sup>22</sup> was used to provide initial guesses for some of the transition state geometries. Intrinsic reaction coordinate (IRC) calculations<sup>23</sup> were used to verify all transition state configurations by tracking the minimum energy paths, leading to adjacent local minima.

Higher level single-point energies were obtained by employing the explicitly correlated coupled-cluster CCSD-(T)-F12a method<sup>24,25</sup> and using an augmented Dunning's correlation consistent, polarized valence triple- $\zeta$  (aug-cc-pVTZ) basis set.<sup>26</sup> Zero-point energy (ZPE) corrections were incorporated into the final energies reported here. Previously, Hwang and Mebel<sup>10</sup> showed that CCSD(T)/6-311G(d,p) level energies are reliable (do not deviate by more than 2 kcal mol<sup>-1</sup> from respective multireference CASSCF calculations using the full valence active space) for similar N/H systems on the  $\text{N}_2\text{H}_4$  potential. The comparison included the iminoammonium ( $\text{NH}_3\text{NH}$ ) species, a zwitterionic compound similar in structure to other zwitterions discussed in the present work. A high value of the  $T_1$  diagnostic parameter<sup>28</sup> implies that additional dynamic electron correlation retrieved by a multireference method could be significant. At the CCSD(T)-F12a/aug-cc-pVTZ level, the  $T_1$  value for  $\text{NH}_3\text{NH}$  is 0.0112, similar to the  $T_1$  range of the various stable species reported in the present work (0.0090–0.0151). However, radicals such as  $\text{N}_2\text{H}_3$  and  $\text{N}_3\text{H}_4$  have higher  $T_1$  values in the range of 0.0211–0.0247, indicating a larger uncertainty in their energies.

Starting from the optimized geometries, separate relaxed potential energy scans were performed as a function of the dihedral angle around each single bond for all stationary points on the PES. All scans had a 10° increment resolution, unless otherwise noted. These hindered rotor (HR) scans were performed using density functional theory employing the Becke-3-Lee-Yang-Parr (B3LYP) functional<sup>29</sup> and the 6-311++G(3df,3pd) basis set.<sup>21</sup> The potential energies were fitted to truncated Fourier series and used as an input to Arkane, an open-source master equation (ME) and transition state theory (TST) solver included within the Reaction Mechanism Generator (RMG) suite,<sup>30,31</sup> to compute the partition functions. The potential scans are given in the [Supporting Information](#) (Figures S1–S10). The optimized geometry was verified to have the lowest energy on these potential scans.

Q-Chem 4.4.0<sup>32</sup> was used for geometry optimizations and frequency calculations. Molpro 2015.1<sup>33,34</sup> was used for coupled-cluster electronic energy calculations. Gaussian<sup>35</sup> was used for all dihedral angle rotor scans, IRC, and GSM calculations. Radical species were computed using unrestricted methods. IQmol<sup>36</sup> was used to plot molecular orbitals generated using the NBO 6.0 population analysis software.<sup>37</sup>

### 2.2. Calculation of Thermodynamic Parameters.

Energies at zero K ( $E_0$ ) of  $\text{n-N}_3\text{H}_5$ ,  $\text{n-N}_3\text{H}_4$ ,  $\text{i-N}_3\text{H}_4$ , and  $\text{n-N}_4\text{H}_6$  were computed at the CCSD(T)-F12/cc-pVTZ-F12 level of theory using geometries optimized at the  $\omega\text{B97x-D3}/6-311++\text{D}(3\text{df},3\text{pd})$  level of theory. Frequencies were calculated at the same level as the geometries, and scaled using a recommended factor of 0.984.<sup>38,39</sup> 1D HR scans were done at the B3LYP/6-311++G(3df,3pd) level of theory. Finally, bond additivity corrections (BACs) were implemented using Arkane.

**2.3. Calculation of Kinetic Parameters.** Both high-pressure ( $P$ ) limit and  $P$ -dependent thermal rate coefficients,  $k(T)$  and  $k(T,P)$ , were calculated at CCSD(T)-F12a/aug-cc-pVTZ// $\omega\text{B97x-D3}/6-311++\text{G}(3\text{df},3\text{pd})$  using Arkane. Values of  $k(T)$  for every elementary chemical reaction which has an energy barrier were calculated by a TST analysis<sup>40</sup> using the rigid-rotor harmonic oscillator (RRHO) approximation with low-energy (<40 kJ mol<sup>-1</sup> barrier) internal rotations modeled as 1D HRs. The effect of internal rotation(s) on the harmonic frequencies was eliminated by projection.<sup>41</sup> One-dimensional asymmetric tunneling through tight transition states was incorporated by assuming that the reaction path can be described by an Eckart function.<sup>42</sup> Phenomenological  $k(T,P)$ 's were computed by applying the microcanonical RRKM (Rice–Ramsperger–Kassel–Marcus) theory to solve the ME<sup>43</sup> under the modified strong collision (MSC) approximation (RRHO and 1D HR approximations were also used in calculating the densities of states).<sup>44</sup> Calculations were performed at a mesh of ( $T_b$ ,  $P_b$ ) points, and the  $k(T_b, P_b)$  was fitted to a Chebyshev polynomial suitable for use in Cantera<sup>45</sup> or the commercial version of CHEMKIN.<sup>46</sup> The reported rate coefficients incorporate appropriate degeneracy factors. For barrierless pathways, high- $P$   $k(T)$ 's estimates (either using literature data or estimated by the respective RMG template) were input into Arkane and converted into  $k(E)$ 's for solution of the ME using an inverse Laplace transform.<sup>44</sup> As is usually done when constructing the ME, the input channel was treated as pseudo-first-order and dissociations into bimolecular products in  $P$ -dependent networks were treated as irreversible. The rate coefficients of collisional energy transfer for deactivating collisions were modeled using the “single exponential down” expression

$$P(E \leftarrow E') \propto \exp\left(-\frac{E' - E}{\langle \Delta E_d \rangle}\right), \quad E' > E$$

where  $\langle \Delta E_d \rangle$  is a measure of the collision efficiency. We computed  $\langle \Delta E_d \rangle$  for  $\text{N}_3\text{H}_5 + \text{N}_2$  and  $\text{N}_4\text{H}_6 + \text{N}_2$  at several temperatures using classical trajectory approaches<sup>47–49</sup> and PES construction strategies<sup>50</sup> described in detail elsewhere. The trajectory-based results are well-represented (to better than 10%) by the expressions  $\langle \Delta E_d \rangle = 175(T/298 \text{ K})^{0.52} \text{ cm}^{-1}$  and  $\langle \Delta E_d \rangle = 250(T/298 \text{ K})^{0.30} \text{ cm}^{-1}$  from  $T = 300$  to 3000 K for  $\text{N}_3\text{H}_5 + \text{N}_2$  and  $\text{N}_4\text{H}_6 + \text{N}_2$ , respectively. The calculated values of  $\langle \Delta E_d \rangle$  for the two systems are similar at high  $T$ , while  $\langle \Delta E_d \rangle$  is larger for  $\text{N}_4\text{H}_6$  than for  $\text{N}_3\text{H}_5$  at low  $T$ . These trends are consistent with those reported previously for hydrocarbons

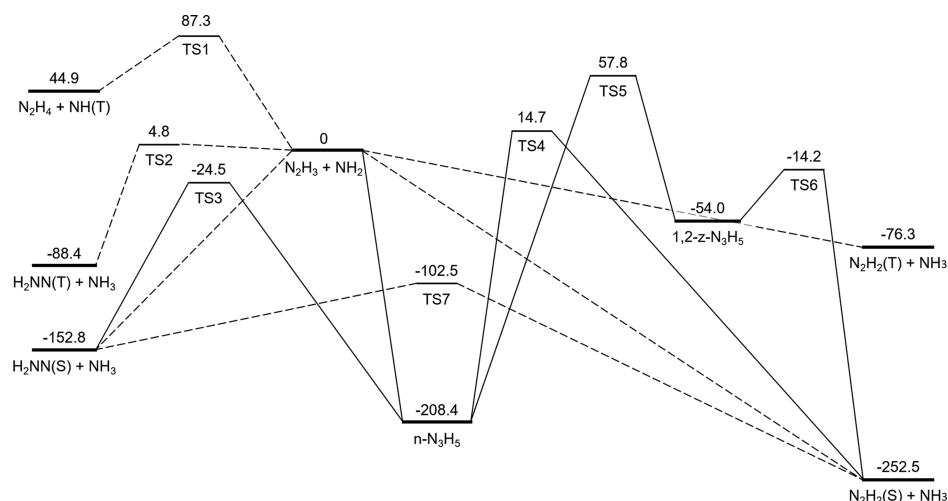


**Figure 1.** Reaction path diagram for the  $\text{N}_3\text{H}_5$  PES. Dashed lines represent nonpressure-dependent pathways. (S) and (T) represent singlet or triplet multiplicities, respectively. Energies are in  $\text{kJ mol}^{-1}$  and scaled relative to the  $\text{N}_2\text{H}_3 + \text{NH}_2$  entry channel, which was set at zero.

and several bath gases,<sup>51</sup> where we also showed that trajectory-based values of  $\langle \Delta E_d \rangle$  often have a weaker temperature dependence than the  $T^{0.85}$  appearing in the empirical standard expression.<sup>52</sup> In addition to uncertainties arising from the value of  $\langle \Delta E_d \rangle$ , errors in the present collision model may be attributed to simplifications in the expression for  $P(E \leftarrow E')$  given above and to the neglect of rovibrational anharmonicity when evaluating the density of states near threshold.<sup>49</sup> Altogether, we often find empirically (e.g., for methane,<sup>53</sup> propargyl radical,<sup>54</sup> and 2-methyl-allyl radical<sup>55</sup>) that the use of the single exponential down model along with trajectory-based values of  $\langle \Delta E_d \rangle$  predicts  $k_0$  with errors of a factor of two or less, thanks in part to a cancellation of errors when rovibrational anharmonicity is neglected.

Transport parameters (Lennard-Jones parameters, dipole moment, and polarizability) were calculated using the OneDMin code,<sup>56</sup> Molpro, and Gaussian. These Lennard-Jones parameters (well depth and collision diameter) are also necessary for pressure-dependent rate coefficient calculations, specifically for the collision frequency calculation. Lennard-Jones parameters were calculated using a DF-MP2/aug-cc-pVDZ PES with  $\text{N}_2$  as the collider. Similar calculations (MP2/aug-cc-pVDZ) were previously shown to be within 10% of the more accurate MP2/CBS and QCISD(T)/CBS computations;<sup>56</sup> similar errors were found in tests of this approach against experimental and higher-level theoretical diffusion coefficients.<sup>57</sup> The dipole moment and polarizability parameters were computed at the B2PLYPD3/cc-pVTZ level. All transport parameters are given in the [Supporting Information](#) (Table S1).

Network sensitivity analysis was conducted using Arkane by perturbing each of the relevant wells and transition states in the PES and determining the effect on the calculated pressure-dependent rate coefficients.

### 3. RESULTS AND DISCUSSION

**3.1.  $\text{N}_3\text{H}_5$  System.** An  $\text{N}_3$  isomer with the empirical chemical formula  $\text{N}_3\text{H}_5$  could be generated in systems with relatively high concentrations of  $\text{N}_2\text{H}_3$  and  $\text{NH}_2$  radicals. This  $\text{N}_3\text{H}_5$  potential energy diagram describes several ammonia-forming pathways (Figure 1). It consists of a pressure-dependent network on the singlet surface (Figure 1) with

two isomers,  $n\text{-N}_3\text{H}_5$  (triazane,  $\text{NH}_2\text{NHNH}_2$ ) and  $1,2\text{-z-N}_3\text{H}_5$  ( $\text{NH}_2\text{NH}_2\text{NH}$ ) (Figure 2), as well as bimolecular pathways on

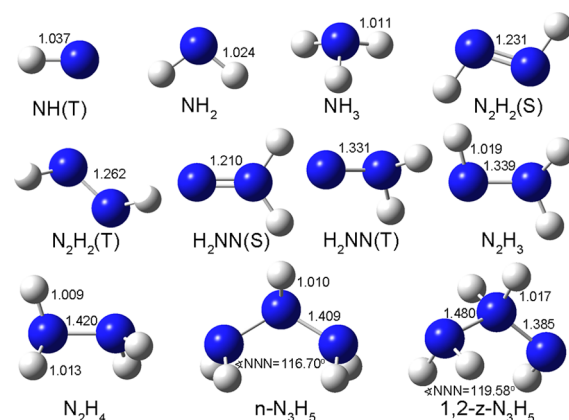


**Figure 2.** Geometric representation of species on the  $\text{N}_3\text{H}_5$  PES optimized at the  $\omega\text{B97x-D3/6-311++G(3df,3pd)}$  level of theory. Bond orders shown for illustration purpose only. Bond lengths are in angstroms and angles in degrees. Quantitative geometric data were added where it benefits the discussion; geometric coordinates for all species are available in the [Supporting Information](#).

both the singlet and triplet surfaces. The “n” and “z” in the species names above stand for normal and zwitterion, respectively. Geometric representations of relevant species and saddle points are given in Figures 2 and 3, respectively. Table 1 lists point groups, rotational constants, and unscaled harmonic frequencies for all relevant species and transition states.

The entry channel of the pressure-dependent network,  $\text{N}_2\text{H}_3 + \text{NH}_2$ , leads via the  $n\text{-N}_3\text{H}_5$  intermediate to two lower-energy bimolecular exit channels, each consisting of an  $\text{N}_2\text{H}_2$  isomer and ammonia. The barrierless high-pressure limit rate coefficient for the complex formation reaction,  $\text{N}_2\text{H}_3 + \text{NH}_2 \leftrightarrow n\text{-N}_3\text{H}_5$  (reaction B1, Table 2), was assumed to equal the rate coefficient of a similar reaction,  $\text{CH}_3\text{NH} + \text{NH}_2 \leftrightarrow \text{CH}_3\text{NHNH}_2$ , calculated at the CASPT2/aug-cc-pVDZ level.<sup>58</sup> For simplicity, highly energetic wells were excluded from the PES. For example,  $\text{N}_2\text{H}_2(\text{S}) + \text{NH}(\text{S})$  formed barrierlessly

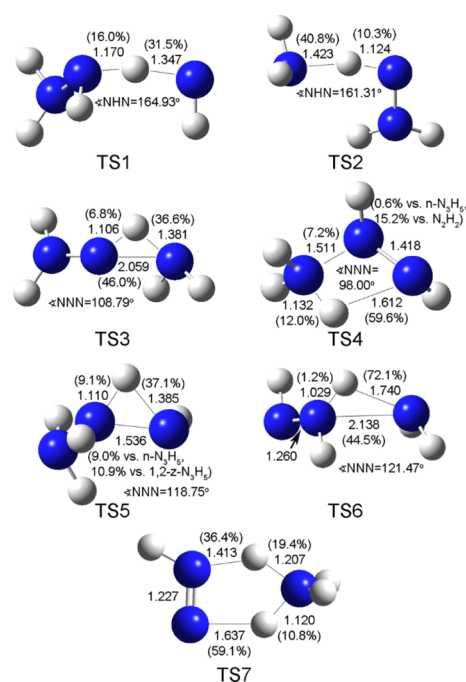


**Figure 3.** Geometric representation of transition states on the  $N_3H_5$  PES optimized at the  $\omega B97x-D3/6-311++G(3df,3pd)$  level of theory. Bond lengths are in angstroms and angles in degrees. Numbers in parentheses indicate the bond stretch fraction relative to the respective stable species. Quantitative geometric data were added where it benefits the discussion; geometric coordinates for all transition states are available in the [Supporting Information](#).

**Table 2.** High-Pressure-Limit Rate Coefficients of Elementary Reactions on the  $N_3H_5$  PES<sup>a</sup>

no. <sup>b</sup>	reaction	$A^c$	$n$	$E_a$ (kJ mol <sup>-1</sup> )	source <sup>d</sup>
R1	$N_2H_4 + NH(T) \leftrightarrow N_2H_3 + NH_2$	$6.09 \times 10^1$	3.61	24.3	pw
R2	$N_2H_3 + NH_2 \leftrightarrow H_2NN(T) + NH_3$	$3.10 \times 10^0$	3.43	−8.2	pw
R3	$n-N_3H_5 \leftrightarrow H_2NN(S) + NH_3$	$1.04 \times 10^{10}$	1.14	177.1	pw
R4	$n-N_3H_5 \leftrightarrow N_2H_2(S) + NH_3$	$1.40 \times 10^9$	0.92	213.3	pw
R5	$n-N_3H_5 \leftrightarrow 1,2-z-N_3H_5$	$7.94 \times 10^9$	0.85	103.9	pw
R6	$1,2-z-N_3H_5 \leftrightarrow N_2H_2(S) + NH_3$	$6.57 \times 10^{11}$	0.57	41.2	pw
R7	$H_2NN(S) + NH_3 \leftrightarrow N_2H_2(S) + NH_3$	$2.07 \times 10^{-1}$	3.64	31.1	pw
B1	$N_2H_3 + NH_2 \leftrightarrow n-N_3H_5$	$5.02 \times 10^{14}$	−0.43	0.2	ref 58
B2	$N_2H_3 + NH_2 \leftrightarrow H_2NN(S) + NH_3$	$3.00 \times 10^{10}$	0.50	0	est., pw
B3	$N_2H_3 + NH_2 \leftrightarrow N_2H_2(S) + NH_3$	$9.20 \times 10^5$	1.94	4.8	ref 62

<sup>a</sup>Parameters are for the modified Arrhenius expression,  $k = AT^n \exp(-E_a/[RT])$ , in the 500–3000 K temperature range; the rate coefficient of reaction B1 is valid in the 200–2500 K temperature range. <sup>b</sup>The R notations refer to reactions as discussed in the text; numbers match the transition states in [Figure 3](#). The B notations refer to barrierless reactions. <sup>c</sup>Units are s<sup>-1</sup> or cm<sup>3</sup> mol<sup>-1</sup> s<sup>-1</sup> for first- or second-order reactions in the forward direction, respectively. <sup>d</sup>pw—calculated in the present work (see text); est.—estimated (see text).

**Table 1.** Point Groups, Rotational Constants, and Unscaled Vibrational Frequencies Calculated at the  $\omega B97x-D3/6-311++G(3df,3pd)$  Level of Theory for Stationary Points on the  $N_3H_5$  PES

stationary point	point group	rotational constants (cm <sup>-1</sup> )		harmonic frequencies (cm <sup>-1</sup> )
NH(T)	$C_{\infty v}$	16.66	3326.8	
NH <sub>2</sub>	$C_{2v}$	23.77, 12.93, 8.37	1519.9, 3418.0, 3510.4	
NH <sub>3</sub>	$C_{3v}$	10.02, 10.02, 6.31	1030.0, 1664.9, 1677.8, 3518.4, 3644.2, 3644.2	
H <sub>2</sub> NN(S)	$C_{2v}$	11.18, 1.34, 1.18	1016.2, 1342.2, 1642.3, 1735.5, 3154.9, 3165.2	
H <sub>2</sub> NN(T)	$C_s$	10.02, 1.13, 1.05	727.2, 1102.3, 1265.6, 1587.7, 3448.1, 3555.2	
N <sub>2</sub> H <sub>2</sub> (S)	$C_{2h}$	10.25, 1.34, 1.18	1351.8, 1355.3, 1601.8, 1701.2, 3309.3, 3335.2	
N <sub>2</sub> H <sub>2</sub> (T)	$C_2$	11.72, 1.17, 1.16	783.5, 1079.8, 1088.7, 1509.7, 3363.1, 3384.5	
N <sub>2</sub> H <sub>3</sub>	$C_1$	6.91, 1.04, 0.91	519.0, 710.8, 1154.5, 1293.8, 1496.0, 1668.8, 3485.1, 3549.2, 3687.8	
N <sub>2</sub> H <sub>4</sub>	$C_2$	4.89, 0.82, 0.82	444.4, 829.7, 973.6, 1154.1, 1311.8, 1342.6, 1681.1, 1693.0, 3515.3, 3524.0, 3619.1, 3623.6	
<i>n</i> -N <sub>3</sub> H <sub>5</sub>	$C_1$	1.37, 0.34, 0.30	334.5, 449.9, 493.8, 824.4, 850.8, 962.2, 1160.4, 1183.5, 1253.9, 1361.3, 1532.8, 1669.9, 1697.6, 3447.3, 3462.0, 3584.0, 3599.0, 3610.7	
1,2- <i>z</i> -N <sub>3</sub> H <sub>5</sub>	$C_1$	1.35, 0.33, 0.30	241.6, 452.6, 482.2, 820.8, 936.0, 982.5, 1169.0, 1203.3, 1403.5, 1457.6, 1504.8, 1645.9, 1671.8, 3357.0, 3466.1, 3482.1, 3520.1, 3559.7	
TS1	$C_1$	1.09, 0.19, 0.17	1900.0i, 25.3, 163.7, 244.1, 463.5, 660.1, 748.7, 844.3, 1163.5, 1175.4, 1363.4, 1443.2, 1557.7, 1667.4, 3380.8, 3520.4, 3561.1, 3661.9	
TS2	$C_1$	1.11, 0.21, 0.18	1229.9i, 164.8, 191.2, 379.7, 542.4, 608.6, 673.5, 878.7, 1079.1, 1262.4, 1297.9, 1498.5, 1553.4, 1632.0, 3444.4, 3499.3, 3535.9, 3655.8	
TS3	$C_1$	1.33, 0.25, 0.22	1409.4i, 232.8, 293.8, 415.5, 557.1, 644.0, 767.8, 812.5, 1221.3, 1346.0, 1515.4, 1569.9, 1690.0, 2568.3, 3503.0, 3522.2, 3619.1, 3627.1	
TS4	$C_1$	1.19, 0.37, 0.31	1194.1i, 286.9, 543.7, 656.7, 847.9, 977.5, 985.2, 1127.7, 1196.8, 1418.5, 1483.3, 1547.7, 1607.4, 2262.6, 3432.7, 3469.5, 3490.7, 3574.8	
TS5	$C_1$	1.37, 0.32, 0.28	1603.4i, 317.7, 362.8, 429.3, 811.7, 914.5, 976.4, 1136.5, 1243.4, 1392.0, 1472.9, 1533.3, 1680.1, 2751.3, 3439.8, 3452.8, 3594.0, 3622.4	
TS6	$C_1$	1.48, 0.22, 0.20	870.5i, 184.6, 284.0, 478.1, 546.1, 632.8, 712.6, 987.4, 1178.4, 1459.8, 1540.9, 1545.8, 1705.5, 3325.9, 3469.7, 3476.7, 3566.4, 3624.4	
TS7	$C_1$	1.18, 0.25, 0.21	1358.0i, 393.8, 453.4, 476.6, 722.7, 752.5, 769.0, 1178.8, 1460.0, 1557.1, 1559.4, 1642.2, 1657.3, 1749.3, 2375.8, 3156.2, 3610.3, 3706.0	



from 1,2-*z*-N<sub>3</sub>H<sub>5</sub> is 192.0 kJ mol<sup>-1</sup> above the N<sub>2</sub>H<sub>3</sub> + NH<sub>2</sub> entry channel.

The N<sub>2</sub>H<sub>2</sub>(S) + NH<sub>3</sub> product well is the most stable product channel in Figure 1, yet the pathway forming the H<sub>2</sub>NN(S) + NH<sub>3</sub> product well has a lower barrier (Figure 1). Nevertheless, all barriers surrounding *n*-N<sub>3</sub>H<sub>5</sub> are relatively high; consequently, even moderate pressures would be enough for the excited complex to be stabilized as *n*-N<sub>3</sub>H<sub>5</sub>.

Iminoammonium (NH<sub>3</sub>NH) and H<sub>2</sub>NNHN were previously shown to be important intermediates in hydrazine decomposition<sup>10,12</sup> and triazene (N<sub>3</sub>H<sub>3</sub>) rearrangements,<sup>59</sup> respectively. Three similar nitrenes on the N<sub>3</sub>H<sub>5</sub> surface could potentially exist, namely, NH<sub>2</sub>NH<sub>2</sub>NH, NH<sub>3</sub>NNH<sub>2</sub>, and NH<sub>3</sub>NHNH, resulting from all possible intrahydrogen transfers in the system. Nevertheless, only NH<sub>2</sub>NH<sub>2</sub>NH (referred to herein as 1,2-*z*-N<sub>3</sub>H<sub>5</sub>, Figure 2) is unimolecularly connected to the entry channel, whereas rearrangements of *n*-N<sub>3</sub>H<sub>5</sub> into NH<sub>3</sub>NNH<sub>2</sub> and NH<sub>3</sub>NHNH immediately lead to bimolecular products (i.e., via TS3 and TS4 in 1,2- and 1,3-NH<sub>3</sub> elimination reactions, respectively).

In addition to recombining to form *n*-N<sub>3</sub>H<sub>5</sub>, N<sub>2</sub>H<sub>3</sub> + NH<sub>2</sub> can also react to directly form bimolecular products without going through the *n*-N<sub>3</sub>H<sub>5</sub> well (see dashed lines in Figure 1). On the singlet surface, disproportionation reactions proceed barrierlessly, forming either N<sub>2</sub>H<sub>2</sub>(S) + NH<sub>3</sub> or H<sub>2</sub>NN(S) + NH<sub>3</sub>. The triplet surface accommodates two hydrogen abstraction reactions via TS1 and TS2, forming N<sub>2</sub>H<sub>4</sub> + NH(T) and H<sub>2</sub>NN(T) + NH<sub>3</sub>, respectively, as well as a barrierless reaction forming N<sub>2</sub>H<sub>2</sub>(T) + NH<sub>3</sub>. The rate coefficient of the barrierless disproportionation reaction N<sub>2</sub>H<sub>3</sub> + NH<sub>2</sub> ↔ H<sub>2</sub>NN(S) + NH<sub>3</sub> (reaction B2 in Table 2) was estimated by ascribing an activation energy of zero to the rate coefficient of the respective nonbarrierless triplet reaction; in this estimation, the rate coefficient of the latter was refitted, constraining its temperature exponent to be 0.5 to obey the collision theory. The rate coefficient of N<sub>2</sub>H<sub>3</sub> + NH<sub>2</sub> ↔ N<sub>2</sub>H<sub>2</sub>(S) + NH<sub>3</sub> was adopted from Dean and Bozzelli<sup>60</sup> (reaction B3 in Table 2). No rate coefficient was assigned for the N<sub>2</sub>H<sub>3</sub> + NH<sub>2</sub> ↔ N<sub>2</sub>H<sub>2</sub>(T) + NH<sub>3</sub> reaction, which leads to the least stable product channel in the system.

We note that optimization efforts of N<sub>3</sub>H<sub>5</sub>(T) at the ωB97x-D3/6-311++G(3df,3pd) level of theory resulted in conformers that could be further stabilized by rotating one of the dihedral angles in the molecule. However, all such rotations (of the two identical rotors) resulted in β-scission of the central hydrogen atom, yielding *i*-N<sub>3</sub>H<sub>4</sub> + H. Because N<sub>3</sub>H<sub>5</sub>(T) rapidly dissociates, intersystem crossing (ISC) behavior in the N<sub>3</sub>H<sub>5</sub> PES is expected to be negligible. Additional ISC effects might play a role in the exit channels of this PES and were not determined within the present framework.

Reactions R1 and R2 (Table 2) describe hydrogen abstractions between N<sub>2</sub>H<sub>3</sub> and NH<sub>2</sub>, where the abstracting radical is different in each reaction. Both transition states, TS1 and TS2 (Figure 3), have similar angles between the atoms participating in the reaction, ∠NHN, of about 160–165°. The reactions are synchronous and the transition states resemble the reactant geometry in the exothermic direction: TS1 has a 16.0% N–H bond stretch fraction relative to N<sub>2</sub>H<sub>4</sub> and a 31.5% stretch relative to NH<sub>2</sub>, whereas TS2 has 10.3 and 40.8% stretches relative to N<sub>2</sub>H<sub>3</sub> and NH<sub>3</sub>, respectively. Bond stretch fractions throughout the discussion are defined as  $(r_{\text{TS}} - r_{\text{stable}})/r_{\text{stable}}$  where  $r_{\text{stable}}$  and  $r_{\text{TS}}$  are the relevant bond lengths in the stable species (either reactant or product, where

this bond exists) and the TS, respectively. In the exothermic direction, reaction R2 has an exceptionally low energy barrier of just 4.8 kJ mol<sup>-1</sup> (Figure 1). It could be explained by the hydrogen bond formed between the nitrogen atom in the abstracting NH<sub>2</sub> group and one of the hydrogen atoms in N<sub>2</sub>H<sub>3</sub>, stabilizing this saddle point (Figure 4).

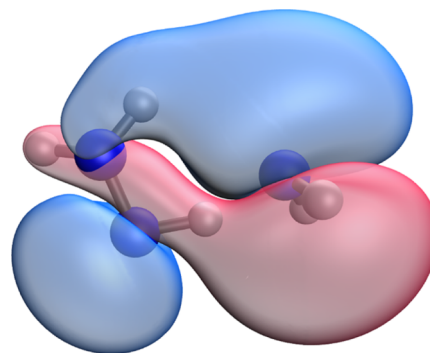


**Figure 4.** Highest  $\alpha$ -electron occupied molecular orbital (MO 12) in the triplet saddle point TS2, computed at the ωB97x-D3/6-311++G(3df,3pd) level of theory.

The transition state of reaction R3, leading to H<sub>2</sub>NN(S) + NH<sub>3</sub> from the *n*-N<sub>3</sub>H<sub>5</sub> isomer via a 1,2-NH<sub>3</sub> elimination route, is asynchronous, characterized by relatively large stretches in both N–N (46.0%) and terminal N–H (36.6%) bonds. These relatively large stretches explain the high  $E_0$  of TS3, 128.3 and 183.9 kJ mol<sup>-1</sup> above the H<sub>2</sub>NN(S) + NH<sub>3</sub> and *n*-N<sub>3</sub>H<sub>5</sub> wells, respectively. The N–H bond stretch fraction in the intermediate nitrogen site, however, is significantly lower (6.8%). The ∠NNN backbone angle is smaller than in the *n*-N<sub>3</sub>H<sub>5</sub> isomer (108.79° vs 116.70°). Indeed, a Mulliken electronic population analysis<sup>61</sup> showed that the reacting NH<sub>2</sub> group (which leaves as NH<sub>3</sub>) and the nonreacting NH<sub>2</sub> group have net formal charges of −0.33 and +0.24, respectively, while each of these groups has a net formal charge of −0.03 in the *n*-N<sub>3</sub>H<sub>5</sub> isomer. The resulting electrostatic attraction forces cause the backbone angle to be smaller than in the isomer.

TS4 is the saddle point of a 1,3-NH<sub>3</sub> elimination reaction of *n*-N<sub>3</sub>H<sub>5</sub>. While the cyclic group in TS3 (describing a 1,2-NH<sub>3</sub> elimination reaction) is −N–H–N–, the geometry of TS4 involves a very strained four-membered ring group, −N–H–N–N–, distorting the molecule backbone. The formed ∠NNN angle in TS4 is significantly smaller than in *n*-N<sub>3</sub>H<sub>5</sub>, only 98.00° versus 116.70°. The N–N bond not directly participating in the reaction (with a bond length of 1.418 Å, Figure 3) is stretched relative to both reactant and product, in accordance with the high strain induced by the cyclic transition: slightly versus *n*-N<sub>3</sub>H<sub>5</sub> (0.6%) and more significantly versus N<sub>2</sub>H<sub>2</sub>(S) (15.2%). As expected from the energetics of the reaction, the length of this bond is more similar to the respective value in *n*-N<sub>3</sub>H<sub>5</sub>. This transition is asynchronous because the hydrogen transfer has significantly progressed (having a 12.0% stretch relative to ammonia and a 59.6% stretch relative to *n*-N<sub>3</sub>H<sub>5</sub>), while the N–N scission has only started (7.2% stretch relative to *n*-N<sub>3</sub>H<sub>5</sub>).

The isomerization pathway via TS5 involves an internal hydrogen transfer between two adjacent nitrogen atoms in *n*-N<sub>3</sub>H<sub>5</sub>; yet unlike TS3, here the intermediate nitrogen atom is a hydrogen acceptor instead of a donor, resulting in a saddle

point raised 82.3 kJ mol<sup>-1</sup> above TS3. In contrast to TS3, the N–N bond is stretched significantly less (9.0% vs n-N<sub>3</sub>H<sub>5</sub> and 10.9% vs 1,2-z-N<sub>3</sub>H<sub>5</sub> compared to 46.0% in TS3) and does not result in scission. The  $\angle$ NNN backbone angle is also intermediate relative to the reacting isomers and slightly closer to the angle in the higher energy nitrene isomer. The distances of the migrating hydrogen with respect to both nitrogen atoms are markedly uneven (9.1% vs 1,2-z-N<sub>3</sub>H<sub>5</sub> and 37.1% vs n-N<sub>3</sub>H<sub>5</sub>); this criterion too suggests a greater resemblance of the saddle point geometry to the nitrene isomer, in accordance with the reaction energetics.

An additional 1,2-NH<sub>3</sub> elimination reaction in this system passes through TS6. Similar to TS3 which belongs to the same reaction family, TS6 is also asynchronous with significant bond stretch fractions with regard to 1,2-z-N<sub>3</sub>H<sub>5</sub> (44.5% N–N stretch) as well as NH<sub>3</sub> (a 72.1% N–H stretch). The large N–H bond stretch fraction is particularly peculiar when compared to the minor N–H bond stretch fraction of the intermediate nitrogen site (only 1.2%), as well as to the respective stretch in TS3 (only 36.6%). Moreover, the N–N bond not directly participating in the reaction is closer in length to the N<sub>2</sub>H<sub>2</sub>(S) product (1.260 Å in TS6 vs 1.231 Å in N<sub>2</sub>H<sub>2</sub>(S) and 1.385 Å in 1,2-z-N<sub>3</sub>H<sub>5</sub>). Finally, the formed  $\angle$ NNN backbone angle is slightly larger than in the reacting isomer (121.47° vs 119.58°), unlike the TS3 case. A Mulliken electronic population analysis of TS6 shows that the reacting NH<sub>2</sub> group and the nonreacting NH group have net formal charges of –0.45 and –0.19, respectively. The resulting electrostatic repulsion forces cause the backbone angle to be wider than in the isomer. It is noted that these groups have net formal charges of +0.12 and –0.43, respectively, in 1,2-z-N<sub>3</sub>H<sub>5</sub>. Calculated high-pressure-limit rate coefficients for the above reactions R1–R6 as well as estimated rate coefficients for barrierless reactions on the N<sub>3</sub>H<sub>5</sub> diagram are given in Table 2.

Reaction R7 catalyzes the H<sub>2</sub>NN(S) to N<sub>2</sub>H<sub>2</sub>(S) transformation using ammonia via a five-membered ring TS. This simultaneous hydrogen transfer TS is asynchronous. The bond lengths of the reacting hydrogens and their neighboring nitrogen atoms suggests an early TS, resembling H<sub>2</sub>NN(S) + NH<sub>3</sub>. Nevertheless, the N–N bond length (1.227 Å) is closer to the respective bond in N<sub>2</sub>H<sub>3</sub>(S) (1.231 Å) rather than to the bond in H<sub>2</sub>NN(S) (1.210 Å).

It is noted that the N<sub>2</sub>H<sub>3</sub> radical has strong coupling between large amplitude fluxional inversion of the amine group and a HR mode (Figure S3). This behavior, characterized by discontinuities in the relaxed potential scan curve due to an abrupt geometry change in the nitrogen backbone, is known to occur in similar systems.<sup>16</sup> A local maximum of ~80 kJ mol<sup>-1</sup>, reached before the inversion point, and a global maximum of ~100 kJ mol<sup>-1</sup> suggest that this mode is significantly hindered. It was therefore not considered as a rotor in any of the calculations in the present work. Although thermodynamic properties of N<sub>2</sub>H<sub>3</sub> are known,<sup>63,64</sup> the authors are not aware of a literature discussion of its 1D HR.

The rate coefficient of reaction R1 (Table 2) was previously estimated by Konnov and De Ruyck<sup>9</sup> based on experimental and theoretical values for other NH(T) + RH  $\leftrightarrow$  NH<sub>2</sub> + R hydrogen abstraction reactions, implementing an activation energy correction based on the Evans–Polanyi correlation. The present calculation and the previous estimation were found to be similar at ~1250 K, yet the Konnov and De Ruyck rate coefficient has a slightly lower temperature dependence despite efforts to adjust its activation energy in that study

(Figure 5). Overall, the disagreement between these rate coefficients is acceptable, considering that one of the rate coefficients is an estimate.

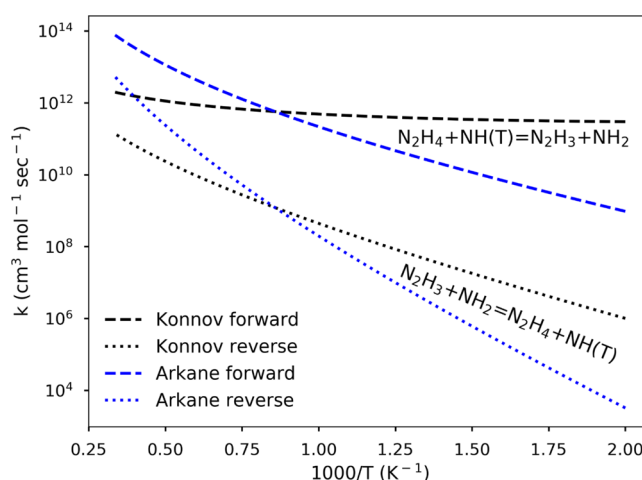


**Figure 5.** Rate coefficient comparisons of reaction R1 (forward) and R-1 (reverse) between the present work calculation using Arkane and the rate coefficient estimated and reported by Konnov and De Ruyck.<sup>9</sup> Thermodynamic data from Curran et al.<sup>64</sup> were used to compute reverse rate coefficients.

As mentioned above, while N<sub>2</sub>H<sub>2</sub>(S) + NH<sub>3</sub> is more stable, the formation route of H<sub>2</sub>NN(S) + NH<sub>3</sub> has a lower barrier (TS3, Figure 1). Indeed, the rate coefficient of the well-skipping reaction N<sub>2</sub>H<sub>3</sub> + NH<sub>2</sub>  $\leftrightarrow$  H<sub>2</sub>NN(S) + NH<sub>3</sub> is orders of magnitude faster than the respective rate coefficient of the competing reaction forming N<sub>2</sub>H<sub>2</sub>(S) throughout the entire temperature and pressure ranges considered here (Figure 6a,b). The RRK (Rice–Ramsperger–Kassel) estimation by Dean and Bozzelli<sup>60</sup> for N<sub>2</sub>H<sub>3</sub> + NH<sub>2</sub>  $\leftrightarrow$  H<sub>2</sub>NN(S) + NH<sub>3</sub> by a well-skipping reaction via n-N<sub>3</sub>H<sub>5</sub> is shown here to overestimate the respective calculated rate coefficients by about 2 orders of magnitude (Figure 6a) because Dean and Bozzelli assumed that TS3 had a lower barrier. Because of higher collisional stabilization of n-N<sub>3</sub>H<sub>5</sub>, the  $k(T,P)$  for N<sub>2</sub>H<sub>3</sub> + NH<sub>2</sub>  $\leftrightarrow$  H<sub>2</sub>NN(S) + NH<sub>3</sub> decreases at high pressures. Interestingly, this rate coefficient is not monotonic with temperature at low pressures (Figure 6a) because this reaction over TS3 is competing with dissociation back to the reactants.

Each of the product channels on this PES could also be formed via bimolecular nonpressure-dependent routes from N<sub>2</sub>H<sub>3</sub> + NH<sub>2</sub>. While the direct route forming N<sub>2</sub>H<sub>2</sub>(S) is faster than the respective well-skipping reaction, the major formation route of H<sub>2</sub>NN(S) is the well-skipping reaction at low pressures and temperatures and it is not negligible at the other studied conditions (Figure 6a,b). Accounting for both unimolecular and bimolecular pathways, H<sub>2</sub>NN(S) formation is favorable over H<sub>2</sub>N<sub>2</sub>(S) in this PES, contrary to a past kinetic stability estimation.<sup>17</sup> Because rate coefficients for both direct routes were estimated (in the present work and by Dean and Bozzelli), further work to determine these values with lower uncertainties is desired.

While 1,2-z-N<sub>3</sub>H<sub>5</sub> formation in this network is negligible (rate coefficients not shown), n-N<sub>3</sub>H<sub>5</sub> formation is significant because of the relatively high barriers surrounding this isomer (Figure 1). As expected, n-N<sub>3</sub>H<sub>5</sub> formation becomes more significant at high pressures because of collisional stabilization

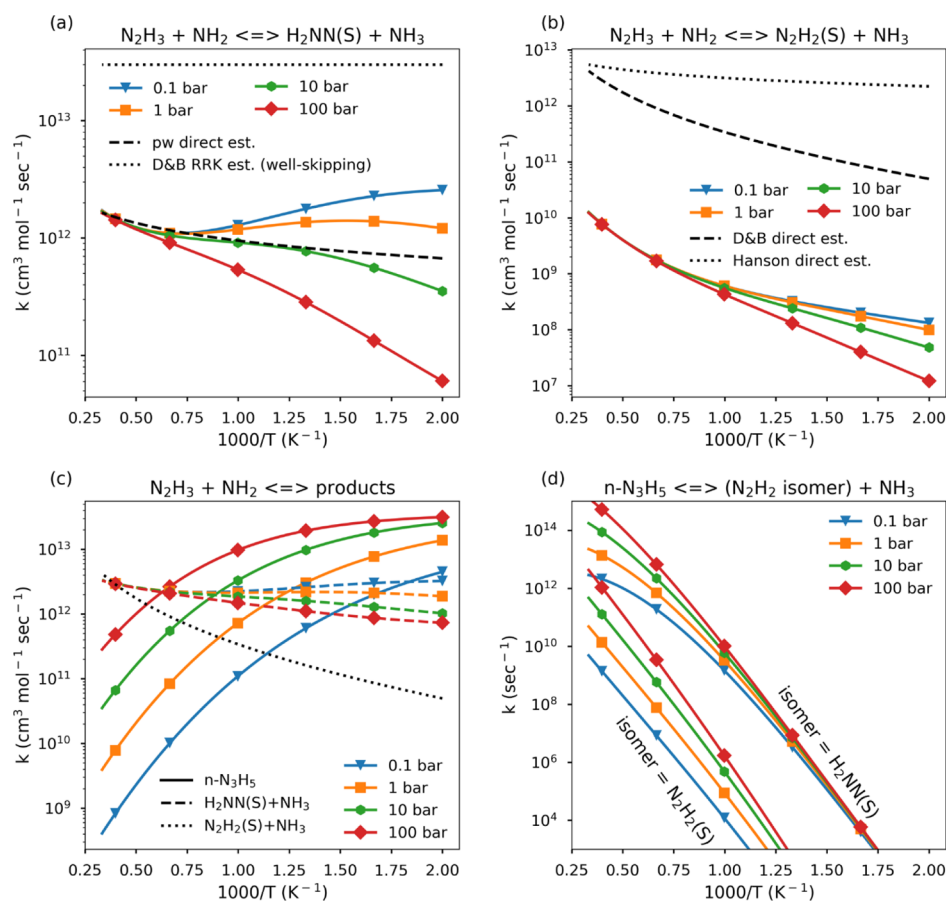


**Figure 6.** Rate coefficient comparisons of selected reactions on the  $\text{N}_3\text{H}_5$  PES. “D&B” in the legend refers to the book chapter by Dean and Bozzelli from 2000,<sup>60</sup> and “Hanson” refers to a N/H/O rate coefficient review by Hanson and Salimian from 1984.<sup>65</sup> The present work is denoted as “pw”. In (c), line types refer to the product/s, while the color refers to the pressure; the pressure dependence of the  $\text{N}_2\text{H}_2(\text{S}) + \text{NH}_3$  formation rate is negligible, while formation rates of  $\text{H}_2\text{NN}(\text{S}) + \text{NH}_3$  include both pressure-dependent and direct routes; the updated Dean and Bozzelli rate coefficient for  $\text{N}_2\text{H}_2(\text{S}) + \text{NH}_3$  is shown.

(Figure 6c). It is also the major product in the network below a pressure-dependent temperature threshold: at 0.1, 1, 10, 25, and 100 bar, this threshold is about 550, 800, 1150, 1250, and 1600 K, respectively. The  $n\text{-N}_3\text{H}_5$  isomer decomposes either while still excited at relatively low pressures if the temperature is high enough, forming preferably  $\text{H}_2\text{NN}(\text{S})$  and  $\text{NH}_3$  (Figure 6d), or after stabilization via hydrogen abstraction reactions mediated by the radical pool (mostly  $\text{H}$ ,  $\text{NH}_2$ , and  $\text{N}_2\text{H}_3$  in hydrazine decomposition systems). All relevant pressure-dependent rate coefficients for this PES are available in the Supporting Information.

A sensitivity analysis of pressure-dependent rate coefficients on the  $\text{N}_3\text{H}_5$  PES was conducted, implementing the chemically significant eigenstate approach.<sup>66,67</sup> This approach is more accurate than the MSC approximation, yet less robust, that is, often fails to converge for relatively large systems. Therefore, only the  $\text{N}_2\text{H}_3 + \text{NH}_2$ ,  $n\text{-N}_3\text{H}_5$ , and  $\text{H}_2\text{NN}(\text{S}) + \text{NH}_3$  wells on the  $\text{N}_3\text{H}_5$  PES were considered for the sensitivity analysis. Results for three selected pressure-dependent reactions, describing  $\text{H}_2\text{NN}(\text{S}) + \text{NH}_3$  formation either via formation of the  $n\text{-N}_3\text{H}_5$  intermediate or skipping the isomer well, are shown (Figure 7).

The sensitivity coefficients for the  $\text{N}_2\text{H}_3 + \text{NH}_2 \leftrightarrow n\text{-N}_3\text{H}_5$  reaction (Figure 7a) suggest that this reaction is in the pressure-dependent “fall-off” region at 1 bar and 1500 K. Increasing  $E_0$  of either the  $\text{N}_2\text{H}_3 + \text{NH}_2$  or the  $n\text{-N}_3\text{H}_5$  wells

changes the density of states around the entry well, increasing or decreasing the rate, respectively. The sensitivity coefficients for  $n\text{-N}_3\text{H}_5$  are lower at the higher pressure because at higher pressures the excited complex lifetime is much shorter, leading to less significant competition from the route via TS3. The  $\text{N}_2\text{H}_3 + \text{NH}_2$  well has a higher sensitivity coefficient at the higher pressure because the leak rate through the submerged barrier TS3 forming  $\text{H}_2\text{NN}(\text{S}) + \text{NH}_3$  is much lower at this condition, and a change in the entrance well  $E_0$  has a larger relative impact.

The  $n\text{-N}_3\text{H}_5 \leftrightarrow \text{H}_2\text{NN}(\text{S}) + \text{NH}_3$  reaction rate has a complex dependency on  $E_0$  of the adduct, the  $\text{N}_2\text{H}_3 + \text{NH}_2$  asymptote, and TS3 (Figure 7b). Perturbing the  $n\text{-N}_3\text{H}_5$  well or the TS3 saddle point results in the expected behavior of the system: increasing  $E_0$  of  $n\text{-N}_3\text{H}_5$  or TS3 increases or decreases the rate, respectively. The system is slightly more sensitive to these parameters at the higher pressure (unlike the previous case) because this is a thermally activated reaction. Increasing  $E_0$  of the  $\text{N}_2\text{H}_3 + \text{NH}_2$  channel results in a slower reverse rate ( $n\text{-N}_3\text{H}_5 \leftrightarrow \text{N}_2\text{H}_3 + \text{NH}_2$ ), changing the branching ratio more in favor of the  $\text{H}_2\text{NN}(\text{S}) + \text{NH}_3$  products. As the pressure increases, the reverse reaction becomes even less favorable, as reflected in the respective sensitivity coefficients at the different pressures.

The rate coefficient of the well-skipping reaction  $\text{N}_2\text{H}_3 + \text{NH}_2 \leftrightarrow \text{H}_2\text{NN}(\text{S}) + \text{NH}_3$  (Figure 7c) is sensitive to the



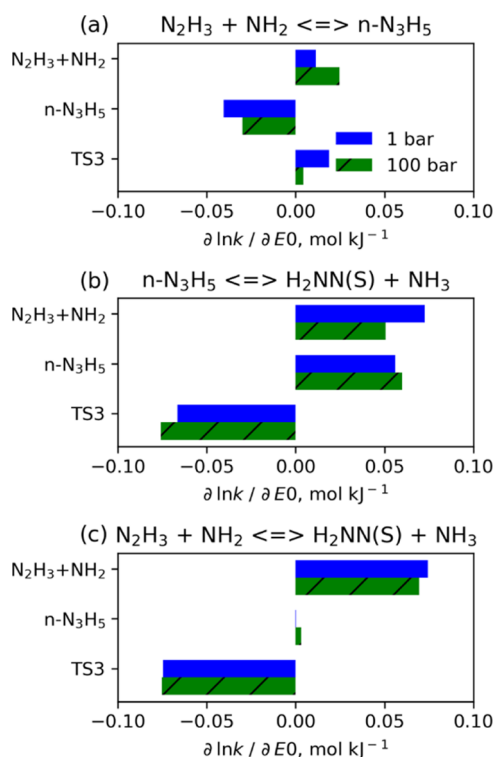


**Figure 7.** Normalized sensitivity coefficients to ZPE-corrected energies of  $\text{N}_2\text{H}_3 + \text{NH}_2$ ,  $n\text{-N}_3\text{H}_5$ , and TS3 for selected pressure-dependent rate coefficients on the  $\text{N}_3\text{H}_5$  potential at 1 and 100 bar and at 1500 K.

energies of the entry channel and transition state, as expected. Increasing  $E_0$  of the entry channel broadens the energy gap between this well and TS3, resulting in a higher rate, while increasing  $E_0$  of TS3 has the opposite effect. This rate coefficient is relatively insensitive to the energy of  $n\text{-N}_3\text{H}_5$ .

The pressure-dependent rate sensitivity analysis allows one to assess the effects of uncertainties in this system. All sensitivity coefficients had values below  $0.1 \text{ mol kJ}^{-1}$ . The sensitivity coefficients of the important  $\text{N}_2\text{H}_3 + \text{NH}_2 \leftrightarrow n\text{-N}_3\text{H}_5$  reaction, which has a significant flux in this system (Figure 6c), were below  $0.05 \text{ mol kJ}^{-1}$ . Therefore, if we can

determine the  $E_0$ 's to within about  $10 \text{ kJ mol}^{-1}$ , the rate coefficient uncertainty due to uncertainties in energies will be less than a factor of 2.

To assess the uncertainties due to estimations of barrierless reaction rate coefficients, we conducted a sensitivity analysis for the pressure-dependent rate coefficient of  $\text{N}_2\text{H}_3 + \text{NH}_2 \leftrightarrow \text{H}_2\text{NN}(\text{S}) + \text{NH}_3$  by perturbing the PES entry channel,  $\text{N}_2\text{H}_3 + \text{NH}_2 \leftrightarrow n\text{-N}_3\text{H}_5$ . At 1, 15, and 80 bar, these normalized (dimensionless) sensitivity coefficients were 0.06, 0.10, and 0.14, respectively. At 15 bar, for example, perturbing the rate coefficient of the barrierless entry channel by factors of 1.05 and 1.50 resulted in 0.5% or 3.4% change, respectively, in the  $k(T, P)$  of  $\text{N}_2\text{H}_3 + \text{NH}_2 \leftrightarrow \text{H}_2\text{NN}(\text{S}) + \text{NH}_3$ .

We note that at high temperatures well merging could add additional uncertainties to the calculated rate coefficients. For example, at high enough temperatures, the  $1,2\text{-z-N}_3\text{H}_5$  isomer could merge with the  $\text{N}_2\text{H}_2(\text{S}) + \text{NH}_3$  product well. Calculating the pressure-dependent rate coefficient of the well-skipping reaction  $\text{N}_2\text{H}_2 + \text{NH}_2 \leftrightarrow \text{N}_2\text{H}_2(\text{S}) + \text{NH}_3$  after forcing the above wells to merge has no significant effect at 1000 K yet reduces the rate by a factor of 1.25 at 3000 K.

**3.2.  $\text{N}_4\text{H}_6$  System.** High  $\text{N}_2\text{H}_3$  concentration may lead to high fluxes on the  $\text{N}_4\text{H}_6$  potential. The  $\text{N}_3\text{H}_5$  and  $\text{N}_4\text{H}_6$  systems are related because  $\text{H}_2\text{NN}(\text{S})$ , a major product of the  $\text{N}_3\text{H}_5$  PES, could react with hydrazine which has a high concentration at early times in the system. The  $\text{N}_2\text{H}_4 + \text{H}_2\text{NN}(\text{S})$  well, in turn, is one of the entry channels on the potential. Nevertheless, it is noted that  $\text{H}_2\text{NN}(\text{S})$  may have more important formation routes such as  $\text{N}_2\text{H}_3$  disproportionation reactions. An additional entry channel on this potential is  $\text{N}_2\text{H}_3 + \text{N}_2\text{H}_3$ . These two channels are interconvertible bimolecularly (Figure 8).

Various non- $P$ -dependent dissociation products could be formed from the two reacting  $\text{N}_2\text{H}_3$  radicals on both the singlet and triplet surfaces, of which the  $\text{N}_2\text{H}_4 + \text{N}_2\text{H}_2(\text{S})$  well is particularly stable. For simplicity, the highly energetic wells  $\text{NH}_3\text{NH} + \text{H}_2\text{NN}(\text{S})$ ,  $\text{NH}_3\text{NH} + \text{H}_2\text{NN}(\text{T})$ , and  $\text{NH}_3\text{NH} + \text{N}_2\text{H}_2(\text{T})$  with energies (on the scale selected for Figure 8) of 183.1, 247.5, and 259.6  $\text{kJ mol}^{-1}$ , respectively, are not shown. Two additional highly energetic product wells of the barrierless reactions  $1,2\text{-z-N}_4\text{H}_6 \leftrightarrow \text{NHNH}_2\text{NH} + \text{NH}_2$  and  $2,3\text{-z-N}_4\text{H}_6 \leftrightarrow \text{NH}_2\text{NH}_2\text{N} + \text{NH}_2$  with energies of 682.7 and 706.4 kJ

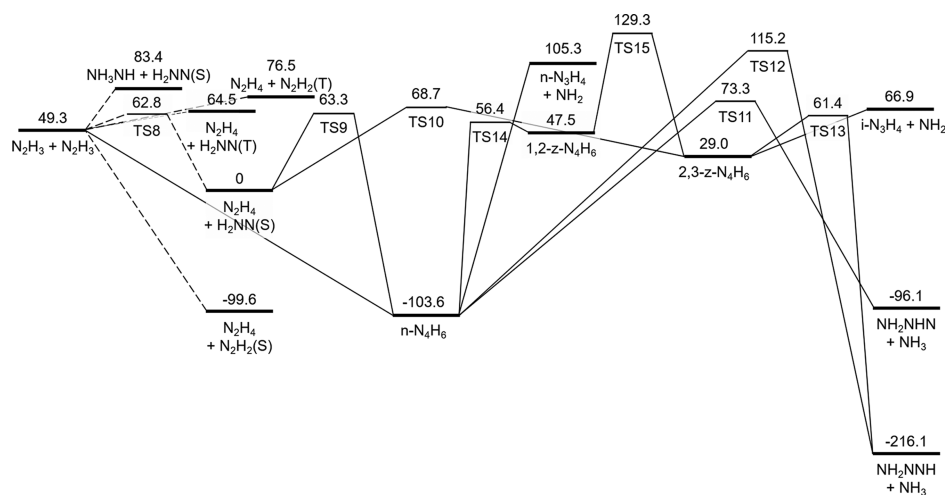


**Figure 8.** Reaction path diagram for the  $\text{N}_4\text{H}_6$  potential. Dashed lines represent nonpressure-dependent pathways. (S) and (T) represent singlet or triplet multiplicities, respectively. Energies are in  $\text{kJ mol}^{-1}$  and scaled relative to the  $\text{N}_2\text{H}_4 + \text{H}_2\text{NN}(\text{S})$  entry channel, which was set to zero.



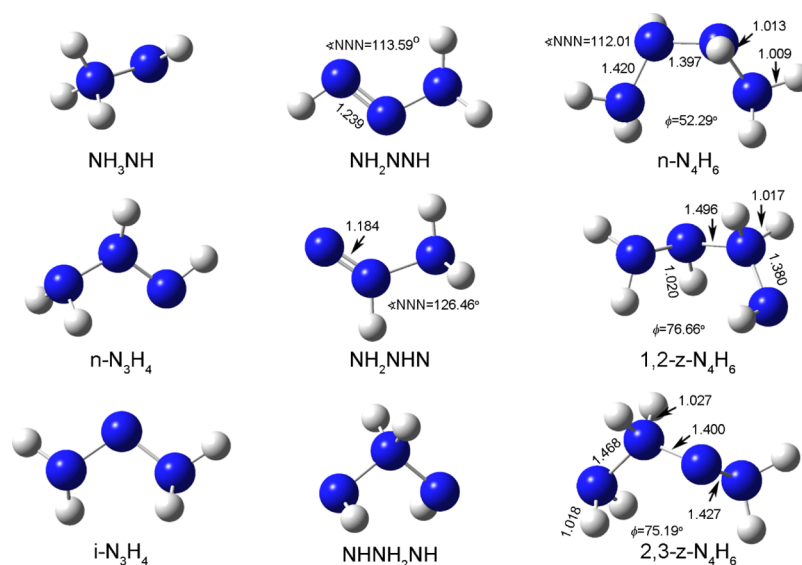


**Figure 9.** Geometric representation of species on the  $N_4H_6$  PES optimized at the  $\omega$ B97x-D3/6-311++G(3df,3pd) level of theory. Species already given in Figure 2 were not reproduced here. Bond orders shown for illustration purpose only. Bond lengths are in angstroms and angles in degrees.  $\phi$  is the dihedral angle between the four nitrogen backbone atoms. Quantitative geometric data were added where it benefits the discussion; geometric coordinates for all species are available in the Supporting Information.

$\text{mol}^{-1}$ , respectively, were excluded. Geometric representations of relevant species and saddle points are given in Figures 9 and 10, respectively. Table S2 lists point groups, rotational constants, and unscaled vibrational frequencies for all relevant species and transition states.

The high-pressure-limit rate coefficient for the entry channel  $N_2H_3 + N_2H_3 \leftrightarrow n-N_4H_6$  (reaction B4, Table 3) was estimated using RMG<sup>30</sup> based on its radical recombination reaction family (“R\_Recombination”). This rate coefficient was estimated to be slower by a factor of 2 with respect to the estimate of Zhang et al. for the similar recombination reaction B1 (Table 2).<sup>58</sup> The high-pressure-limit rate coefficients for the exit channels  $n-N_4H_6 \leftrightarrow n-N_3H_4 + NH_2$ ,  $1,2-z-N_4H_6 \leftrightarrow NHNH_2NH + NH_2$ , and  $2,3-z-N_4H_6 \leftrightarrow i-N_3H_4 + NH_2$  (reactions B5–B7) were estimated similarly using the radical recombination family in RMG. All high-pressure-limit rate coefficients are given in Table 3. The respective microcanonical rate coefficients were calculated by Arkane using an inverse Laplace transform.

The pressure-dependent network on the singlet surface potential has three stable isomers,  $n-N_4H_6$  (tetrazane),  $1,2-z-N_4H_6$ , and  $2,3-z-N_4H_6$  (Figures 8 and 9). Similar to the  $N_3H_5$  case, additional zwitterionic isomers could theoretically be thought of, yet only the two isomers listed above and illustrated in Figure 9 were found to be connected to the network by isomerizations. Most of the saddle points on the  $N_4H_6$  potential are located within a relatively narrow energy range of 56.4–73.3  $\text{kJ mol}^{-1}$  above  $N_2H_4 + H_2NN(S)$  (Figure 8), making the various transitions quite competitive. The two exceptions are TS12 and TS15 with relatively high energies, which are expected to significantly inhibit the flux through the respective channels.

Consequently, an interesting phenomenon emerges where a different entry channel would favor a different final product. A chemically activated complex formed by a  $N_2H_4 + H_2NN(S)$  collision could form  $n-N_4H_6$  via TS9 or  $2,3-z-N_4H_6$  via TS10. The energized  $n-N_4H_6$  is likely to either be collisionally stabilized or rapidly dissociate to form two  $N_2H_3$  radicals,

depending on the pressure and temperature. If  $2,3-z-N_4H_6$  is formed via TS10, it will rapidly dissociate to form either  $i-N_3H_4 + NH_2$  or  $NH_2NNH + NH_3$ .

On the other hand, an excited complex formed by a  $N_2H_3 + N_2H_3$  collision will most likely be collisionally stabilized, forming  $n-N_4H_6$ , or dissociate back to  $N_2H_3 + N_2H_3$ . The alternative pathways for continued reaction via TS9 or TS11 or the barrierless dissociation to  $n-N_3H_4 + NH_2$  are all significantly uphill compared to the  $N_2H_3 + N_2H_3$  entry channel. Note that the  $N_2H_3 + N_2H_3$  and  $N_2H_4 + H_2NN(S)$  entry channels are interconvertible bimolecularly via a relatively low energy saddle point, TS8, but  $N_2H_3 + N_2H_3$  is more likely to undergo barrierless disproportionation to  $N_2H_3 + N_2H_2(S)$ .

TS8 is the saddle point of the  $N_2H_3 + N_2H_3$  disproportionation reaction forming  $N_2H_4 + H_2NN(S)$ . It is an early and synchronous transition state, as expected from the reactant and product energetics. It is noted that this reaction was found to be intrinsically different from a similar reaction on the  $N_3H_5$  potential,  $N_2H_3 + NH_2 \leftrightarrow H_2NN(S) + NH_3$  (reaction B2, Table 2), where the latter was determined to be barrierless.

TS9, a saddle point of a nitrene insertion into an N–N bond, is asynchronous. Most interestingly, the N–N bond length in the substructure originated from  $N_2H_4$  is shorter than the respective bond lengths in both the reactant  $N_2H_4$  and the product  $n-N_4H_6$  (1.379 vs 1.420 and 1.397 Å, respectively). TS8 and TS9 are geometrically and energetically similar (Figures 8 and 10). The major difference between these geometries is the orientation of the terminal hydrogens not directly participating in the reaction, which causes the complex to either recombine or fall apart because of electrostatic forces.

The addition reaction  $N_2H_4 + H_2NN(S) \leftrightarrow 2,3-z-N_4H_6$  passes through TS10. This TS has a similar geometry to the product except the central N–N bond which has stretched significantly. It is an asynchronous transition in which the N–N bond length of the  $H_2NN(S)$  reactant stretches considerably (81.6% stretch fraction) before reaching the saddle point, while the N–N bond length of the  $N_2H_4$  reactant hardly stretches

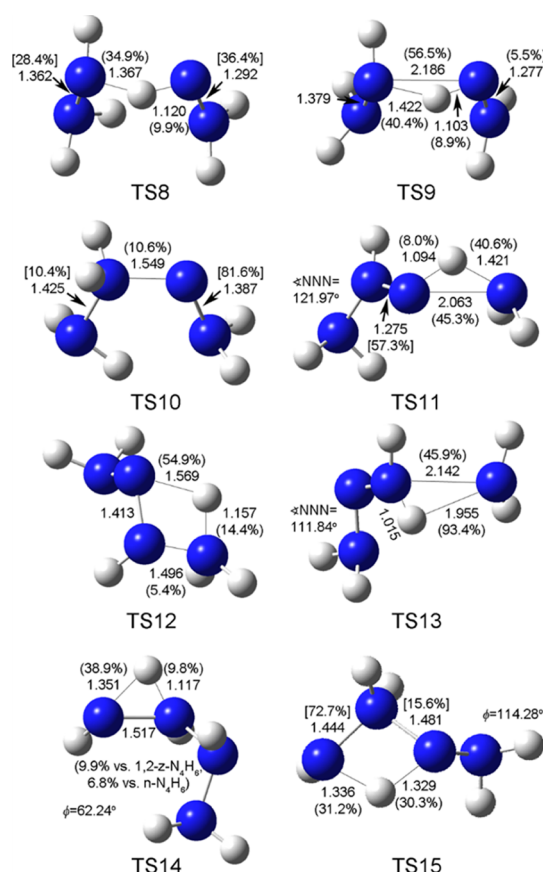


**Figure 10.** Geometric representation of transition states on the  $N_4H_6$  PES optimized at the  $\omega B97x-D3/6-311++G(3df,3pd)$  level of theory. Bond lengths are in angstroms and angles in degrees. Numbers in parentheses indicate the bond stretch fraction relative to the respective stable species. Numbers in brackets indicate the relative bond stretch fraction out of the total change between the respective reactant and product in the direction specified in Table 3.  $\phi$  is the dihedral angle between the four nitrogen backbone atoms. Quantitative geometric data were added where it benefits the discussion; geometric coordinates for all transition states are available in the Supporting Information.

(10.4% stretch fraction). Relative bond stretch fractions throughout the discussion are defined as  $(r_{TS} - r_{reactant}) / (r_{product} - r_{reactant})$ , where  $r_{reactant}$ ,  $r_{product}$ , and  $r_{TS}$  are the relevant bond lengths in the reactant, product, and the TS, respectively.

Two reactions of the 1,2- $NH_3$  elimination family on this potential pass through transition states TS11 and TS13. In both cases, the  $\angle NNN$  backbone angles of the forming products in the TS are close to the values of the stable  $NH_2NHN$  and  $NH_2NNH$  products, respectively. Both are asynchronous, primarily characterized by a highly stretched N–N bond of the leaving  $NH_2$  group (45.3 and 93.4%, respectively) and a low stretch of the N–H bond to be ruptured. In fact, the respective N–H bond in TS13 is shorter than in the reactant, and overall the geometry and energies indicate that  $NH_2$  was nearly dissociated but grabbed an H atom as it departed. Methods developed for roaming reactions<sup>68</sup> may be helpful for better evaluating this rate coefficient.

A 1,3- $NH_3$  elimination reaction on this surface,  $n-N_4H_6 \leftrightarrow NH_2NNH + NH_3$ , has a strained four-membered ring transition geometry, TS12. This transition state is also

**Table 3.** High-Pressure-Limit Rate Coefficients of Elementary Reactions on the  $N_4H_6$  PES<sup>a</sup>

no. <sup>b</sup>	reaction	$A^c$	$n$	$E_a$ (kJ mol <sup>−1</sup> )	source <sup>d</sup>
R8	$N_2H_3 + N_2H_3 \leftrightarrow N_2H_4 + H_2NN(S)$	$1.11 \times 10^{-1}$	3.21	−1.5	pw
R9	$N_2H_4 + H_2NN(S) \leftrightarrow n-N_4H_6$	$4.73 \times 10^{-1}$	3.55	50.6	pw
R10	$N_2H_4 + H_2NN(S) \leftrightarrow 2,3-z-N_4H_6$	$2.29 \times 10^0$	2.96	55.4	pw
R11	$n-N_4H_6 \leftrightarrow NH_2NHN + NH_3$	$3.00 \times 10^{12}$	0.83	178.7	pw
R12	$n-N_4H_6 \leftrightarrow NH_2NNH + NH_3$	$7.70 \times 10^{10}$	0.84	214.1	pw
R13	$2,3-z-N_4H_6 \leftrightarrow NH_2NNH + NH_3$	$4.03 \times 10^{13}$	0.26	38.7	pw
R14	$n-N_4H_6 \leftrightarrow 1,2-z-N_4H_6$	$7.90 \times 10^{11}$	0.59	158.6	pw
R15	$1,2-z-N_4H_6 \leftrightarrow 2,3-z-N_4H_6$	$1.74 \times 10^{10}$	0.91	74.4	pw
B4	$N_2H_3 + N_2H_3 \leftrightarrow n-N_4H_6$	$2.51 \times 10^{14}$	−0.43	0.2	est., pw
B5	$n-N_3H_4 + NH_2 \leftrightarrow n-N_4H_6$	$5.02 \times 10^{14}$	−0.43	0.2	est., pw
B6	$NHNH_2NH + NH_2 \leftrightarrow 1,2-z-N_4H_6$	$5.02 \times 10^{14}$	−0.43	0.2	est., pw
B7	$i-N_3H_4 + NH_2 \leftrightarrow 2,3-z-N_4H_6$	$1.17 \times 10^{16}$	−1.26	2.8	est., pw
B8	$N_2H_3 + N_2H_3 \leftrightarrow N_2H_4 + N_2H_2(S)$	$1.20 \times 10^{13}$	0	0	ref 9

<sup>a</sup>Parameters are for the modified Arrhenius expression,  $k = AT^n \exp(-E_a/[RT])$ , in the 500–3000 K temperature range. <sup>b</sup>The R notations refer to reactions as discussed in the text; numbers match the transition states in Figure 10. The B notations refer to barrierless reactions. <sup>c</sup>Units are s<sup>−1</sup> or cm<sup>3</sup> mol<sup>−1</sup> s<sup>−1</sup> for first- or second-order reactions in the forward direction, respectively. <sup>d</sup>pw—calculated in the present work (see text); est.—estimated (see text).

asynchronous with the central N–N bond stretched relative to both reactants and products and a small  $\angle NNN$  ring angle of 98.78°, all of which are similar characteristics to TS4 (Figure 3).

TS14 and TS15 are saddle points of isomerization reactions on this surface:  $n-N_4H_6 \leftrightarrow 1,2-z-N_4H_6$  and  $1,2-z-N_4H_6 \leftrightarrow 2,3-z-N_4H_6$ . Note that no direct reaction was identified between  $n-N_4H_6$  and  $2,3-z-N_4H_6$ . Exhaustive searches for such saddle point always lead to dissociation of the complex into  $N_2H_4$  and  $H_2NN(S)$ , as this pathway resembles the geometry of TS9 (Figure 10). The transition geometry of TS14 is synchronous and late as expected from the reaction energetics. Facilitating the internal hydrogen transfer in this reaction causes the N–N bond over which this transfer occurs to stretch relative to both relevant isomers. The geometry of TS15, on the other hand, is asynchronous; although the hydrogen stretches nearly evenly on both sides (30.3 and 31.2%), the outer N–N bond stretches considerably (72.7% relative bond stretch fraction), whereas the internal N–N bond stretches slightly (15.6% relative bond stretch fraction).

The  $n-N_4H_6$  formation rate is higher when entering from the  $N_2H_3 + N_2H_3$  channel, compared to  $N_2H_4 + H_2NN(S)$  (Figure 11), because of the relatively high energy barrier in the later (Figure 8). As expected, more  $n-N_4H_6$  is formed with respect to both entry channels as the pressure increases. The rate coefficient of the estimated reaction B4 (Table 3) is within a factor of 2 from the rate coefficient of the calculated and comparable reaction B1 (Table 2) forming  $n-N_3H_5$  for all studied conditions (Figures 6c and 11).

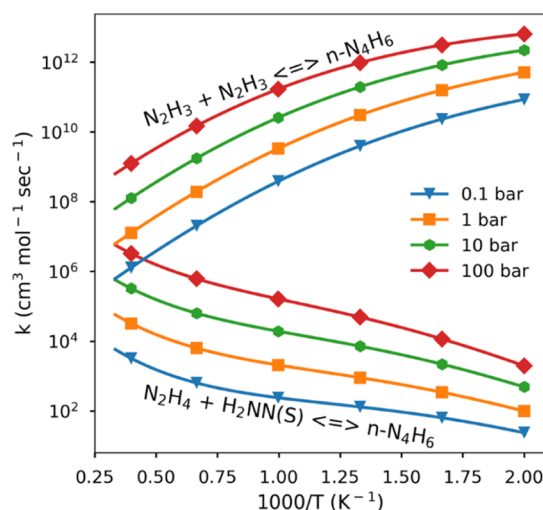


**Figure 11.** Rate coefficient comparison of  $n\text{-N}_4\text{H}_6$  formation from each of the entry channels as a function of temperature and pressure.

Rate coefficient comparison starting from each of the entry channels on the  $\text{N}_4\text{H}_6$  potential suggests a single dominant product channel,  $\text{N}_2\text{H}_4 + \text{N}_2\text{H}_2(\text{S})$ , though at high pressures  $n\text{-N}_4\text{H}_6$  formation is comparable;  $\text{N}_2\text{H}_4 + \text{H}_2\text{NN}(\text{S})$  would preferably form  $\text{N}_2\text{H}_3 + \text{N}_2\text{H}_3$  (Figure 12a), which in turn mostly yield  $\text{N}_2\text{H}_4 + \text{N}_2\text{H}_2(\text{S})$  (Figure 12b). The tendency of  $\text{N}_2\text{H}_3$  radicals to react via a disproportionation route rather than recombine to form  $n\text{-N}_4\text{H}_6$  was previously observed experimentally at 298 K and low pressure, and a branching ratio of four was determined.<sup>19</sup> Our calculated rate coefficient for the recombination reaction R9 at these conditions ( $3.0 \times 10^{12} \text{ cm}^3 \text{ mol}^{-1} \text{ s}^{-1}$ ) is a factor of 3.3 lower than the disproportionation rate coefficient (reaction R8) estimated by Konnov and De Ruyck,<sup>9</sup> in accordance with the experimental observation. Consequently, the experimental observation along with the present calculations suggests that the rate coefficient of reaction B8 could not be much lower than the value suggested by Konnov and De Ruyck<sup>9</sup> at these conditions. The gap between the rates of the two routes is shown here to increase with temperature and decrease with pressure. At relatively high pressures and low temperatures,  $n\text{-N}_4\text{H}_6$

formation becomes significant, yet at the conditions relevant to hydrazine decomposition (1500 K and 25 bar), the formation rate of tetrazane from  $\text{N}_2\text{H}_3$  recombination is 2 orders of magnitude lower than the formation rate of the disproportionation products,  $\text{N}_2\text{H}_4 + \text{N}_2\text{H}_2(\text{S})$ . Also of importance are reactions yielding  $n\text{-N}_3\text{H}_4 + \text{NH}_2$  and  $\text{NH}_2\text{NNH} + \text{NH}_3$ , while formation rates of  $\text{NH}_2\text{NNH} + \text{NH}_3$  and  $i\text{-N}_3\text{H}_4 + \text{NH}_2$  from the  $\text{N}_2\text{H}_3 + \text{N}_2\text{H}_3$  entry channel are negligible (Figure S11), in accordance with the above discussion.

**3.3. Thermodynamic Properties.** The present work emphasizes the importance of accounting for triazane ( $n\text{-N}_3\text{H}_5$ ) when kinetically studying hydrazine decomposition systems (Figure 6c). Tetrazane ( $n\text{-N}_4\text{H}_6$ ) formation in this system only becomes important at high pressures and relatively low temperatures (Figure 12) because of fall-off into  $\text{N}_2\text{H}_3 + \text{N}_2\text{H}_3$ . The main decomposition pathways of triazane are formation of  $\text{H}_2\text{NN}(\text{S}) + \text{NH}_3$  at high temperatures (Figure 6d), as well as hydrogen abstraction reactions because of interactions with the radical pool (mainly  $\text{H}$ ,  $\text{NH}_2$ , and  $\text{N}_2\text{H}_3$ ). The latter results in the formation of primary or secondary radicals,  $n\text{-N}_3\text{H}_4$  or  $i\text{-N}_3\text{H}_4$ , respectively (Figure 9). Preliminary RMG predictions suggest that the  $n\text{-N}_3\text{H}_4$  radical primarily decomposes into  $\text{NH}_2 + \text{N}_2\text{H}_2(\text{S})$  via a  $\beta$ -scission reaction, whereas the  $i\text{-N}_3\text{H}_4$  radical primarily abstracts a hydrogen atom from  $\text{N}_2\text{H}_2(\text{S})$ , forming  $n\text{-N}_3\text{H}_5 + \text{NNH}$ . Consequently,  $n\text{-N}_3\text{H}_5$ ,  $n\text{-N}_3\text{H}_4$ , and  $i\text{-N}_3\text{H}_4$  should all be considered in future kinetic models of similar systems.

Thermodynamic properties were computed using Arkane at the CCSD(T)-F12a/cc-pVTZ-F12// $\omega\text{B97x-D3/6-311+G-(3df,3pd)}$  level of theory (Table 4). The  $T_1$  diagnostic parameters<sup>28</sup> calculated at the CCSD(T)-F12a/cc-pVTZ-F12 level of theory for  $n\text{-N}_3\text{H}_5$ ,  $n\text{-N}_3\text{H}_4$ ,  $i\text{-N}_3\text{H}_4$ , and  $n\text{-N}_4\text{H}_6$  are 0.0102, 0.0232, 0.0209, and 0.0107, respectively. The  $n\text{-N}_3\text{H}_4$  and  $i\text{-N}_3\text{H}_4$  radicals have strong coupling between large amplitude fluxional inversion and HR modes (Figures S6 and S7), which makes it challenging to compute their heat capacities. Therefore, only RRHO enthalpies and entropies at 298 K are reported for these radicals.

The calculated standard heat of formation and entropy of formation of  $n\text{-N}_3\text{H}_5$  (Table 4) are comparable with respective past values calculated using the G2 method,<sup>69</sup> 198.7 kJ mol<sup>-1</sup>

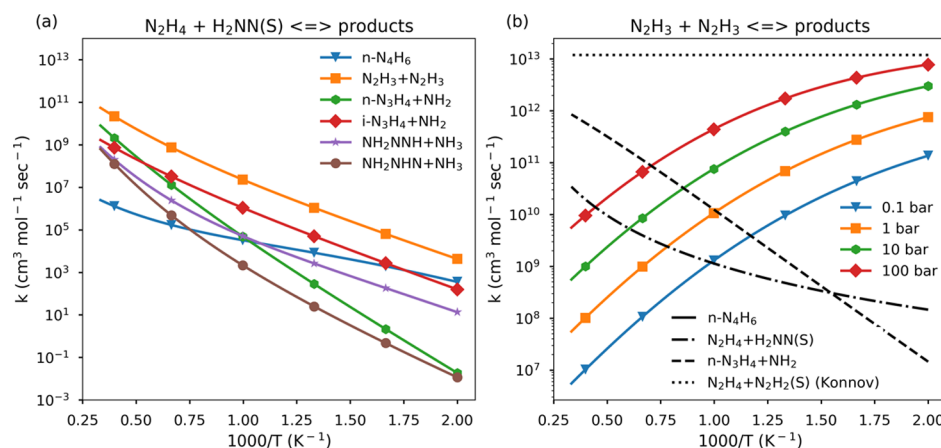


**Figure 12.** Rate coefficient comparisons of  $\text{N}_2\text{H}_4 + \text{H}_2\text{NN}(\text{S})$  and  $\text{N}_2\text{H}_3 + \text{N}_2\text{H}_3$  reactions. Rates in (a) are given at a representative pressure of 10 bar. In (b), line types refer to the product/s, while the color refers to the pressure; the pressure-dependent rate for  $n\text{-N}_3\text{H}_4 + \text{NH}_2$  formation via a well-skipping reaction is negligible; the rate for  $\text{N}_2\text{H}_4 + \text{H}_2\text{NN}(\text{S})$  formation includes both the direct route (via TS8) and the well-skipping route; the dotted line is an estimated rate by Konnov and De Ruyck.<sup>9</sup>



**Table 4. Thermodynamic Properties of n-N<sub>3</sub>H<sub>5</sub>, n-N<sub>3</sub>H<sub>4</sub>, i-N<sub>3</sub>H<sub>4</sub>, and n-N<sub>4</sub>H<sub>6</sub> at the CCSD(T)-F12a/cc-pVTZ-F12// $\omega$ B97x-D3/6-311++G(3df,3pd) Level of Theory<sup>a</sup>**

species	$\Delta H_f^\circ$	$\Delta S_f^\circ$	$C_p(T)^b$								
			300 K	400 K	500 K	600 K	800 K	1000 K	1500 K	2000 K	2400 K
n-N <sub>3</sub> H <sub>5</sub>	203.3	276.9	75.1	86.3	95.5	103.7	117.3	128.0	145.7	155.9	161.3
n-N <sub>3</sub> H <sub>4</sub>	322.5	274.1									
i-N <sub>3</sub> H <sub>4</sub>	289.6	262.7									
n-N <sub>4</sub> H <sub>6</sub>	299.7	289.8	80.6	99.4	115.2	128.6	150.4	166.6	191.5	205.4	213.3

<sup>a</sup>Enthalpies are given in kJ mol<sup>-1</sup>; entropies and constant pressure heat capacities are given in J mol<sup>-1</sup> K<sup>-1</sup>. <sup>b</sup>No  $C_p$  values are reported for the N<sub>3</sub>H<sub>4</sub> radicals, see text.

and 261.5 J mol<sup>-1</sup> K<sup>-1</sup>, respectively.<sup>17</sup> The NASA polynomials for the thermodynamic properties of triazane and tetrazane are given in the [Supporting Information](#).

#### 4. CONCLUSIONS

A detailed kinetic analysis of the N<sub>3</sub>H<sub>5</sub> and N<sub>4</sub>H<sub>6</sub> potentials was presented. On the N<sub>4</sub>H<sub>6</sub> potential, the N<sub>2</sub>H<sub>4</sub> + H<sub>2</sub>NN(S) entry channel mostly yields N<sub>2</sub>H<sub>3</sub> + N<sub>2</sub>H<sub>3</sub>, while the N<sub>2</sub>H<sub>3</sub> + N<sub>2</sub>H<sub>3</sub> channel, in turn, would primarily result in the formation of N<sub>2</sub>H<sub>4</sub> + N<sub>2</sub>H<sub>2</sub>(S) by direct disproportionation. Overall, hydrazine on this surface mainly catalyzes isomer transformation from H<sub>2</sub>NN(S) to N<sub>2</sub>H<sub>2</sub>(S). At high pressures and low temperatures, tetrazane (n-N<sub>4</sub>H<sub>6</sub>) formation becomes significant.

Starting from the N<sub>2</sub>H<sub>3</sub> + NH<sub>2</sub> entry channel, all bimolecular product wells on the N<sub>3</sub>H<sub>5</sub> potential can be reached directly via a bimolecular reaction. In fact, the rate contribution of the well-skipping pathway forming N<sub>2</sub>H<sub>2</sub>(S) + NH<sub>3</sub> to the overall rate is negligible, while the well-skipping route forming H<sub>2</sub>NN(S) + NH<sub>3</sub> has a significant contribution and dominates in the low-pressure and low-temperature regime. Starting from N<sub>2</sub>H<sub>3</sub> + NH<sub>2</sub>, H<sub>2</sub>NN(S) formation is kinetically more favorable than N<sub>2</sub>H<sub>2</sub>(S) under 2500 K. Triazane (n-N<sub>3</sub>H<sub>5</sub>) becomes the dominant product of N<sub>2</sub>H<sub>3</sub> + NH<sub>2</sub> reaction below 550, 800, 1150, 1250, and 1600 K at 0.1, 1, 10, 25, and 100 bar, respectively. Triazane is predicted to form either H<sub>2</sub>NN(S) + NH<sub>3</sub> or primary/secondary N<sub>3</sub>H<sub>4</sub> radicals, all of which should be taken into consideration in kinetic models of hydrazine.

Theoretical predictions of reaction rate coefficients have been derived from ab initio TST coupled with ME simulations as necessary. The determined pressure-dependent rates should be of considerable utility to future efforts of kinetic modeling of hydrazine decomposition and related systems.

#### ■ ASSOCIATED CONTENT

##### Supporting Information

The Supporting Information is available free of charge on the ACS Publications website at DOI: [10.1021/acs.jpca.9b02217](https://doi.org/10.1021/acs.jpca.9b02217).

Transport properties, stationary point properties, relaxed rotor scans, branching ratios of N<sub>2</sub>H<sub>3</sub> + N<sub>2</sub>H<sub>3</sub>, NASA polynomials for n-N<sub>3</sub>H<sub>5</sub> and n-N<sub>4</sub>H<sub>6</sub>, geometric coordinates, and pressure-dependent rates ([PDF](#))

#### ■ AUTHOR INFORMATION

##### Corresponding Author

\*E-mail: [whgreen@mit.edu](mailto:whgreen@mit.edu). Phone: +1-617-253-4580. Fax: +1-617-324-0066.

##### ORCID

Alon Grinberg Dana: [0000-0001-7545-8719](https://orcid.org/0000-0001-7545-8719)

Ahren W. Jasper: [0000-0003-0216-9347](https://orcid.org/0000-0003-0216-9347)

William H. Green: [0000-0003-2603-9694](https://orcid.org/0000-0003-2603-9694)

##### Notes

The authors declare no competing financial interest.

#### ■ ACKNOWLEDGMENTS

This overall project was funded primarily by the Gas Phase Chemical Physics Program of the US Department of Energy, Office of Basic Energy Sciences, Division of Chemical Sciences, Geosciences, and Biosciences (under award number DE-SC0014901). A.G.D. was supported by The George J. Elbaum Scholarship in Engineering, The Ed Satell Foundation, and The Zuckerman STEM Leadership Program. K.B.M. was supported by the Army Research Office under award number W911NF1710531. A.W.J. was supported by the US Department of Energy, Office of Basic Energy Sciences, Division of Chemical Sciences, Geosciences, and Biosciences through Argonne National Laboratory (DE-AC02-06CH11357). All financial support is gratefully acknowledged. We thank Dr. Hiroumi Tani from Japan Aerospace Exploration Agency (JAXA) for helpful conversations.

#### ■ REFERENCES

- (1) Rothgery, E. F. Hydrazine and its Derivatives. *Kirk-Othmer Encyclopedia of Chemical Technology*, 2004; Vol. 13.
- (2) Gray, P.; Lee, J. C.; Spencer, M. Combustion, flame and explosion of hydrazine and ammonia I-The spontaneous ignition of pure gaseous hydrazine. *Combust. Flame* **1963**, 7, 315–321.
- (3) Auzanneau, M.; Roux, M. Self-Detonation Range in Inert Atmosphere of Ternary Systems Using Hydrogen Peroxide and Hydrazine or Hydrazine Derivatives. *Combust. Sci. Technol.* **1990**, 73, 505–520.
- (4) *Dynamics of Detonations and Explosions: Detonations*; Leyer, J.-C., Borisov, A. A., Kuhl, A. L., Sirignano, W. A., Eds.; American Institute of Aeronautics and Astronautics: Washington DC, 1991.
- (5) Rath, M.; Schmitz, H.; Steenborg, M. Development of a 400 N Hydrazine Thruster for ESA's Atmospheric Reentry Demonstrator. *32nd Joint Propulsion Conference and Exhibit*; American Institute of Aeronautics and Astronautics: Reston, Virginia, 1996.
- (6) Yang, A.-S.; Kuo, T.-C. Design Analysis of a Satellite Hydrazine Propulsion System. *J. Propuls. Power* **2002**, 18, 270–279.
- (7) Anflo, K.; Mollerberg, R.; Neff, K.; King, P. High Performance Green Propellant for Satellite Applications. *45th AIAA/ASME/SAE/ASEE Joint Propulsion Conference and Exhibit*; American Institute of Aeronautics and Astronautics: Reston, Virginia, 2009.
- (8) Halat-Augier, C.; Dupre, G.; Paillard, C. E. Thermal Decomposition of Gaseous Hydrazine behind a Reflected Shock Wave. *Proceedings of the 20th International Symposium on Shock Waves*, 1996; Vol. 2, pp 893–943.
- (9) Konnov, A. A.; De Ruyck, J. Kinetic Modeling of the Decomposition and Flames of Hydrazine. *Combust. Flame* **2001**, 124, 106–126.

- (10) Hwang, D.-Y.; Mebel, A. M. Reaction Mechanism of  $\text{N}_2/\text{H}_2$  conversion to  $\text{NH}_3$ : A Theoretical Study. *J. Phys. Chem. A* **2003**, *107*, 2865–2874.
- (11) Klippenstein, S. J.; Harding, L. B.; Ruscic, B.; Sivaramakrishnan, R.; Srinivasan, N. K.; Su, M.-C.; Michael, J. V. Thermal Decomposition of  $\text{NH}_2\text{OH}$  and Subsequent Reactions: Ab Initio Transition State Theory and Reflected Shock Tube Experiments. *J. Phys. Chem. A* **2009**, *113*, 10241–10259.
- (12) Asatryan, R.; Bozzelli, J. W.; Silva, G. d.; Swinnen, S.; Nguyen, M. T. Formation and Decomposition of Chemically Activated and Stabilized Hydrazine. *J. Phys. Chem. A* **2010**, *114*, 6235–6249.
- (13) Wiberg, N.; Bayer, H.; Bachhuber, H. Isolation of Tetrazene,  $\text{N}_4\text{H}_4$ . *Angew. Chem., Int. Ed.* **1975**, *14*, 177–178.
- (14) Zhao, M.; Gimarc, B. M. Strain Energies of  $(\text{NH})_n$  Rings,  $n = 3$ –8. *J. Phys. Chem.* **1994**, *98*, 7497–7503.
- (15) Inagaki, S.; Ishitani, Y.; Kakefu, T. Geminal Delocalization of  $\sigma$ -Electrons and Ring Strains. *J. Am. Chem. Soc.* **1994**, *116*, 5954–5958.
- (16) Ball, D. W. High-Level Ab Initio Calculations on Hydrogen-Nitrogen Compounds. Thermochemistry of Tetrazetidine,  $\text{N}_4\text{H}_4$ . *J. Mol. Struct.: THEOCHEM* **2002**, *619*, 37–43.
- (17) Schlegel, H. B.; Skancke, A. Thermochemistry, energy comparisons, and conformational analysis of hydrazine, triazane, and triaminoammonia. *J. Am. Chem. Soc.* **1993**, *115*, 7465–7471.
- (18) Ball, D. W. Tetrazane: Hartree–Fock, Gaussian-2 and -3, and Complete Basis Set Predictions of Some Thermochemical Properties of  $\text{N}_4\text{H}_6$ . *J. Phys. Chem. A* **2001**, *105*, 465–470.
- (19) Stief, L. J. Ratio of Disproportionation to Combination of  $\text{N}_2\text{H}_3$  Radicals. *J. Chem. Phys.* **1970**, *52*, 4841–4845.
- (20) Lin, Y.-S.; Li, G.-D.; Mao, S.-P.; Chai, J.-D. Long-Range Corrected Hybrid Density Functionals with Improved Dispersion Corrections. *J. Chem. Theory Comput.* **2013**, *9*, 263–272.
- (21) Krishnan, R.; Binkley, J. S.; Seeger, R.; Pople, J. A. Self-consistent molecular orbital methods. XX. A basis set for correlated wave functions. *J. Chem. Phys.* **1980**, *72*, 650–654.
- (22) Zimmerman, P. M. Growing String Method with Interpolation and Optimization in Internal Coordinates: Method and Examples. *J. Chem. Phys.* **2013**, *138*, 184102.
- (23) Gonzalez, C.; Schlegel, H. B. An Improved Algorithm for Reaction Path Following. *J. Chem. Phys.* **1989**, *90*, 2154–2161.
- (24) Adler, T. B.; Knizia, G.; Werner, H.-J. A Simple and Efficient CCSD(T)-F12 Approximation. *J. Chem. Phys.* **2007**, *127*, 221106.
- (25) Knizia, G.; Adler, T. B.; Werner, H.-J. Simplified CCSD(T)-F12 Methods: Theory and Benchmarks. *J. Chem. Phys.* **2009**, *130*, 054104.
- (26) Dunning, T. H. Gaussian Basis Sets for Use in Correlated Molecular Calculations. I. The Atoms Boron through Neon and Hydrogen. *J. Chem. Phys.* **1989**, *90*, 1007–1023.
- (27) Computational Chemistry Comparison and Benchmark Database; National Institute of Standards and Technology (NIST), U.S. Department of Commerce. Available online <https://cccbdb.nist.gov/vibscalejust.asp> (last accessed April 2019).
- (28) Lee, T. J.; Rice, J. E.; Scuseria, G. E.; Schaefer, H. F. Theoretical Investigations of Molecules Composed Only of Fluorine, Oxygen and Nitrogen: Determination of the Equilibrium Structures of FOOF,  $(\text{NO})_2$  and FNNF and the Transition State Structure for FNNF Cis-Trans Isomerization. *Theor. Chim. Acta* **1989**, *75*, 81–98.
- (29) Becke, A. D. Density-functional thermochemistry. III. The role of exact exchange. *J. Chem. Phys.* **1993**, *98*, 5648–5652.
- (30) Gao, C. W.; Allen, J. W.; Green, W. H.; West, R. H. Reaction Mechanism Generator: Automatic Construction of Chemical Kinetic Mechanisms. *Comput. Phys. Commun.* **2016**, *203*, 212–225.
- (31) Reaction Mechanism Generator, RMG-Py v2.3.0. <https://github.com/ReactionMechanismGenerator/RMG-Py>, 2019.
- (32) Shao, Y.; Gan, Z.; Epifanovsky, E.; Gilbert, A. T. B.; Wormit, M.; Kussmann, J.; Lange, A. W.; Behn, A.; Deng, J.; Feng, X.; et al. Advances in Molecular Quantum Chemistry Contained in the Q-Chem 4 Program Package. *Mol. Phys.* **2015**, *113*, 184–215.
- (33) Werner, H.-J.; Knowles, P. J.; Knizia, G.; Manby, F. R.; Schütz, M. Molpro: A General-Purpose Quantum Chemistry Program Package. *Wiley Interdiscip. Rev.: Comput. Mol. Sci.* **2012**, *2*, 242–253.
- (34) Werner, H.-J.; Knowles, P. J.; Knizia, G.; Manby, F. R.; Schütz, M.; Celani, P.; Györffy, W.; Kats, D.; Korona, T.; Lindh, R.; et al. Molpro, Version 2015.1, a Package of Ab Initio Programs, Cardiff, UK, 2015.
- (35) Frisch, M. J.; Trucks, G. W.; Schlegel, H. B.; Scuseria, G. E.; Robb, M. A.; Cheeseman, J. R.; Montgomery, J. A.; Vreven, T.; Kudin, K. N.; Burant, J. C.; et al. Gaussian 03, Revision D.01; Gaussian, Inc.: Wallingford, CT, 2009.
- (36) Gilbert, A. IQmol, Version 2.11. <http://iqmol.org/>, 2018.
- (37) Glendening, E. D.; Badenhop, J. K.; Reed, A. E.; Carpenter, J. E.; Bohmann, J. A.; Morales, C. M.; Landis, C. R.; Weinhold, F. NBO 6.0; Theoretical Chemistry Institute, University of Wisconsin: Madison, 2013.
- (38) Bao, J. L.; Zheng, J.; Alecu, I. M.; Lynch, B. J.; Zhao, Y.; Truhlar, D. G. Database of Frequency Scale Factors for Electronic Model Chemistries, 2016. <https://comp.chem.umn.edu/freqscale/version3b2.htm>.
- (39) Alecu, I. M.; Zheng, J.; Zhao, Y.; Truhlar, D. G. Computational Thermochemistry: Scale Factor Databases and Scale Factors for Vibrational Frequencies Obtained from Electronic Model Chemistries. *J. Chem. Theory Comput.* **2010**, *6*, 2872–2887.
- (40) Truhlar, D. G.; Garrett, B. C.; Klippenstein, S. J. Current Status of Transition-State Theory. *J. Phys. Chem.* **1996**, *100*, 12771–12800.
- (41) Wong, B. M.; Green, W. H. Effects of Large-Amplitude Torsions on Partition Functions: Beyond the Conventional Separability Assumption. *Mol. Phys.* **2005**, *103*, 1027–1034.
- (42) Eckart, C. The Penetration of a Potential Barrier by Electrons. *Phys. Rev.* **1930**, *35*, 1303–1309.
- (43) Kislov, V. V.; Mebel, A. M.; Aguilera-Iparraguirre, J.; Green, W. H. Reaction of Phenyl Radical with Propylene as a Possible Source of Indene and Other Polycyclic Aromatic Hydrocarbons: An Ab Initio/RRKM-ME Study. *J. Phys. Chem. A* **2012**, *116*, 4176–4191.
- (44) Allen, J. W.; Goldsmith, C. F.; Green, W. H. Automatic Estimation of Pressure-Dependent Rate Coefficients. *Phys. Chem. Chem. Phys.* **2012**, *14*, 1131–1155.
- (45) Goodwin, D. G.; Moffat, H. K.; Speth, R. L. Cantera: An Object-Oriented Software Toolkit for Chemical Kinetics, Thermodynamics, and Transport Processes, 2018.
- (46) CHEMKIN-PRO 15131, Reaction Design, San Diego, 2013.
- (47) Jasper, A. W.; Miller, J. A. Collisional Energy Transfer in Unimolecular Reactions: Direct Classical Trajectories for  $\text{CH}_4 \rightleftharpoons \text{CH}_3 + \text{H}$  in Helium. *J. Phys. Chem. A* **2009**, *113*, 5612–5619.
- (48) Jasper, A. W.; Miller, J. A.; Klippenstein, S. J. Collision Efficiency of Water in the Unimolecular Reaction  $\text{CH}_4 (+\text{H}_2\text{O}) \rightleftharpoons \text{CH}_3 + \text{H} (+\text{H}_2\text{O})$ : One-Dimensional and Two-Dimensional Solutions of the Low-Pressure-Limit Master Equation. *J. Phys. Chem. A* **2013**, *117*, 12243–12255.
- (49) Jasper, A. W.; Pelzer, K. M.; Miller, J. A.; Kamarchik, E.; Harding, L. B.; Klippenstein, S. J. Predictive a Priori Pressure-Dependent Kinetics. *Science* **2014**, *346*, 1212–1215.
- (50) Jasper, A. W.; Davis, M. J. Parameterization Strategies for Intermolecular Potentials for Predicting Trajectory-Based Collision Parameters. *J. Phys. Chem. A* **2019**, *123*, 3464–3480.
- (51) Jasper, A. W.; Oana, C. M.; Miller, J. A. "Third-Body" collision efficiencies for combustion modeling: Hydrocarbons in atomic and diatomic baths. *Proc. Combust. Inst.* **2015**, *35*, 197–204.
- (52) Greenwald, E. E.; North, S. W.; Georgievskii, Y.; Klippenstein, S. J. A Two Transition State Model for Radical–Molecule Reactions: A Case Study of the Addition of OH to  $\text{C}_2\text{H}_4$ . *J. Phys. Chem. A* **2005**, *109*, 6031–6044.
- (53) Jasper, A. W.; Miller, J. A. Theoretical Unimolecular Kinetics for  $\text{CH}_4 + \text{M} \rightleftharpoons \text{CH}_3 + \text{H} + \text{M}$  in Eight Baths,  $\text{M} = \text{He}, \text{Ne}, \text{Ar}, \text{Kr}, \text{H}_2, \text{N}_2, \text{CO}$ , and  $\text{CH}_4$ . *J. Phys. Chem. A* **2011**, *115*, 6438–6455.
- (54) Klippenstein, S. J.; Miller, J. A.; Jasper, A. W. Kinetics of Propargyl Radical Dissociation. *J. Phys. Chem. A* **2015**, *119*, 7780–7791.

- (55) Tranter, R. S.; Jasper, A. W.; Randazzo, J. B.; Lockhart, J. P. A.; Porterfield, J. P. Recombination and Dissociation of 2-Methyl Allyl Radicals: Experiment and Theory. *Proc. Combust. Inst.* **2017**, *36*, 211–218.
- (56) Jasper, A. W.; Miller, J. A. Lennard-Jones parameters for combustion and chemical kinetics modeling from full-dimensional intermolecular potentials. *Combust. Flame* **2014**, *161*, 101–110.
- (57) Jasper, A. W.; Kamarchik, E.; Miller, J. A.; Klippenstein, S. J. First-Principles Binary Diffusion Coefficients for H, H<sub>2</sub>, and Four Normal Alkanes + N<sub>2</sub>. *J. Chem. Phys.* **2014**, *141*, 124313.
- (58) Zhang, P.; Klippenstein, S. J.; Sun, H.; Law, C. K. Ab Initio Kinetics for the Decomposition of Monomethylhydrazine (CH<sub>3</sub>NHNH<sub>2</sub>). *Proc. Combust. Inst.* **2011**, *33*, 425–432.
- (59) Förstel, M.; Tsegaw, Y. A.; Maksyutenko, P.; Mebel, A. M.; Sander, W.; Kaiser, R. I. On the Formation of N<sub>3</sub>H<sub>3</sub> Isomers in Irradiated Ammonia Bearing Ices: Triazene (H<sub>2</sub>NNNH) or Triimide (HNHNH). *ChemPhysChem* **2016**, *17*, 2726–2735.
- (60) Dean, A. M.; Bozzelli, J. W. Combustion Chemistry of Nitrogen. *Gas-Phase Combustion Chemistry*; Springer: New York, NY, 2000; pp 125–341.
- (61) Mulliken, R. S. Electronic Population Analysis on LCAO-MO Molecular Wave Functions. I. *J. Chem. Phys.* **1955**, *23*, 1833–1840.
- (62) Chang, A. Y.; Bozzelli, J. W.; Dean, A. M. Kinetic Analysis of Complex Chemical Activation and Unimolecular Dissociation Reactions Using QRRK Theory and the Modified Strong Collision Approximation. *Z. Phys. Chem.* **2000**, *214*, 1533.
- (63) Simmie, J. M. A Database of Formation Enthalpies of Nitrogen Species by Compound Methods (CBS-QB3, CBS-APNO, G3, G4). *J. Phys. Chem. A* **2015**, *119*, 10511–10526.
- (64) Bugler, J.; Somers, K. P.; Simmie, J. M.; Güthe, F.; Curran, H. J. Modeling Nitrogen Species as Pollutants: Thermochemical Influences. *J. Phys. Chem. A* **2016**, *120*, 7192–7197.
- (65) Hanson, R. K.; Salimian, S. Survey of Rate Constants in the N/H/O System. *Combustion Chemistry*; Springer: New York, NY, 1984; pp 361–421.
- (66) Klippenstein, S. J.; Miller, J. A. From the Time-Dependent, Multiple-Well Master Equation to Phenomenological Rate Coefficients. *J. Phys. Chem. A* **2002**, *106*, 9267–9277.
- (67) Miller, J. A.; Klippenstein, S. J. Master Equation Methods in Gas Phase Chemical Kinetics. *J. Phys. Chem. A* **2006**, *110*, 10528–10544.
- (68) Prozument, K.; Suleimanov, Y. V.; Buesser, B.; Oldham, J. M.; Green, W. H.; Suits, A. G.; Field, R. W. A Signature of Roaming Dynamics in the Thermal Decomposition of Ethyl Nitrite: Chirped-Pulse Rotational Spectroscopy and Kinetic Modeling. *J. Phys. Chem. Lett.* **2014**, *5*, 3641–3648.
- (69) Curtiss, L. A.; Raghavachari, K.; Trucks, G. W.; Pople, J. A. Gaussian-2 theory for molecular energies of first- and second-row compounds. *J. Chem. Phys.* **1991**, *94*, 7221–7230.